Towards the "Waiting-Point" Nucleus ^{129}Ag

Y. Jading

univer
sität
mainz

Towards
the "Waiting-Point" Nucleus
^{129}Ag

Dissertation zur Erlangung des Grades
"Doktor der Naturwissenschaften"

am Fachbereich Physik
der Johannes Gutenberg–Universität
in Mainz

Ylva Jading
geboren in Västervik

Mainz 1996

Abstract

The astrophysical rapid-neutron capture process, r-process, is responsible for the nucleo-synthesis of a large part of all elements heavier than iron. Using the "waiting-point" model the r-abundances can be predicted by only using three nuclear and three stellar input parameters. For a given set of stellar parameters the neutron-separation energies S_n determine the r-process path; the β-decay halflives $T_{1/2}$ of the nuclei in the r-process path define the progenitor abundances and taking the neutron emission probabilities P_n into account also the final r-abundances. Of particular importance are the neutron-magic waiting-point isotopes. For instance, are the N = 82 progenitor isotopes responsible for the A $\simeq$ 130 solar r-abundance peak.

This thesis is concerned with the identification and investigation of neutron-rich silver isotopes and in particular the neutron-magic waiting-point nucleus ^{129}Ag. Creating and detecting very neutron-rich nuclei is a complicated and time-consuming process, if at all possible. A main problem with these silver experiments, which were carried out at the CERN-ISOLDE facility, is the high isobaric background. To decrease the In contamination a laser ion source based on chemically-selective photo ionization was developed. However, up to now the neutron-magic ^{129}Ag isotope has not be identified but improvements of the production system give reason to be optimistic for the future.

Nevertheless, a number of new neutron-rich isotopes, $^{125-128}$Ag, have been observed in the two experiments which have already taken place. Based on the nuclear data presented in this thesis it can be seen that the proton-neutron interaction, as expected, plays an important role in understanding the structure of these nuclei. This is due to the large overlap between the wave-functions of the $\nu g_{7/2}$ and $\pi g_{9/2}$ single-particle levels which gives rise to a dramatic lowering of the $\nu g_{7/2}$ level as the $\pi g_{9/2}$ orbit is filled.

Observing the experimental trends from the measured halflives for the neutron-rich silver isotopes it can be seen that the theoretical prediction for $T_{1/2}(^{129}\text{Ag})$ is too long. This contradicts earlier halflife measurements on ^{130}Cd which could be well correlated with the solar abundances. It is not enough to only take the thermal population of the $\pi p_{1/2}$ isomer into account. It seems that the situation for the neutron capture in ^{128}Ag can be well explained by capture in states above the S_n in ^{129}Ag. From these capture states γ-decay to both levels, $\pi p_{1/2}$ and $\pi g_{9/2}$, can occur and in this way the required stellar halflife would be described by a mixture of the $T_{1/2}$ from the two isomers.

This thesis also contains an quantitative evaluation of the biases in the chi-square fit methods. They are of special importance in analysis of low statistics, which cannot be assumed to be normal distributed.

Contents

Chapter 1

Introduction

Humans through the ages have tried to explain how the world was created. The quality of these explanations has been improved with the sophistication of the observation methods. In our time the methods of observing the universe have become more advanced than ever. Satellites and world-wide observatory nets help us to constantly increase our information about the cosmos. However, we have also learned that it is possible to gain new knowledge about cosmic processes by studying the microscopic reactions which are the energy sources keeping up these processes. It is, for example, of vital importance that it is energetically favourable for our sun to convert enormous amounts of hydrogen fuel into helium. The fact that macro and micro cosmos are closely linked together offers new possibilities of gaining information about the universe from the world of nuclei and particles. With the help of accelerators we can today revive material no longer existing in the universe and in this way get snapshots of periods long-since lost. We can create and examine exotic nuclei, which normally only exist in stars and in this way, among other things, find clues as to the creation of matter the way we know it. The relation between macro and micro cosmos can also be used the opposite way, to improve our knowledge on subatomic physics using cosmic data.

This thesis is concerned with the nuclear properties of waiting-point nuclei occurring in the astrophysical rapid-neutron capture process, the r-process. This is the process which together with the slow-neutron capture process, the s-process, and the rapid proton capture process, the p-process, synthesize all elements heavier than iron. The r-process is solely responsible for elements heavier than bismuth. The p-process is little known up to now but it is assumed to synthesize some proton-rich nuclei which cannot be produced by the s- or r-process. The s-process synthesizes nuclei along the valley of stability. Each neutron capture along the process path takes typically 10 years but the following beta decay is normally much faster. In this way, the s-process synthesizes the elements between iron, the seed nuclei, and bismuth. The s-process can take place in a helium burning environment with stellar temperatures of $1.8 - 3.2 \cdot 10^8$ K and neutron densities of $0.8 - 1.8 \cdot 10^8$ cm^{-3} [Bee88].

The r-process, on the other hand, goes through isotopes near the neutron dripline. There the neutron capture occurs on a time scale of ms and beta decay is typically slower, except in the *waiting-point nuclei* when the neutron capture takes long enough to allow beta decay. However, when a neutron-magic isotope is reached it is not that favourable for the

nucleus to absorb another neutron and start a new neutron shell. The isotope then has time to beta decay and can then add one more neutron to again become neutron magic. In this way, the path comes so close to stability so the time scale for beta decay will allow the neutron capture of the first neutron in the next shell. Once this is done, the following neutron captures are considerably faster and the path returns to the region close to the neutron dripline. The r-process takes place during extreme conditions, concerning stellar temperature, neutron density and time scale. Typical values are, according to recent calculations, temperatures of $1 - 3 \cdot 10^9$ K, neutron number densities of $10^{20} - 10^{25}$ cm^{-3} and a process duration in the order of two seconds [Kra93]. Several astrophysical sites have been proposed for the r-process over the years and today supernovae type II or SNII are a fairly accepted site. Recently it has been proposed that the r-process should take place in a high-entropy environment in delayed core-collapse SNII [Mey92]. This hot bubble assumes that an evacuated zone is created in the outer region of the core between the stalled shockwave and the collapsed inner part of the core. At high entropy conditions most of the protons will be bound in alpha particles. Then a rather moderate neutron-to-proton ratio of about 1.6 will leave enough free neutrons per seed nucleus. In order to synthesize uranium from iron, some $100 - 130$ neutrons per seed are needed. This scenario has the advantage that the release of the required amount of r-process material from supernovae can be easier explained than in older SNII core models. Despite its importance, the r-process is not yet fully understood. This is to a large extent due to the fact that only very few isotopes in its path can be observed in terrestrial laboratories. In order to reach a better understanding of this nucleosynthesis process more nuclear data are needed.

Complete network calculations of the r-process element abundances require a large number of astrophysical and nuclear-physics input parameters. However, theoretical calculations can be considerably simplified by assuming the classical (n,γ)$\rightleftharpoons$(γ,n)-equilibrium [B^{2}FH57] in combination with a local steady β-flow. In this approach, the nuclear input parameters can be limited to the nuclear masses, or neutron-separation energies, S_n, beta decay halflives, $T_{1/2}$, and beta-delayed neutron emission probabilities, P_n, of the isotopes in the r-process path. In addition, the following stellar parameters have to be provided, temperature, T_9, neutron density, n_n, and process duration, τ. For a given n_n the S_n determine the r-process path, the $T_{1/2}$ of the isotopes along this flow path, in principle, define the progenitor abundances and, when taking P_n branching into account, also the final r-abundances. Of particular importance are the neutron-magic waiting-point isotopes. For instance, the N = 82 progenitor isotopes are responsible for the A $\simeq$ 130 solar r-abundance, $N_{r,\odot}$, peak. It is, therefore, of great interest to measure the beta decay properties of the neutron-magic ^{130}Cd, ^{129}Ag and ^{128}Pd isotopes.

This thesis contains a description of the two first beamtimes of the silver experiment, IS333, and a nickel production test. The experiments described were carried out at the CERN-ISOLDE mass separator. The nickel production test has been including in this thesis although, up to now, it has not been followed by a proposal for an experiment. The reason for this is that it has many things in common with the silver experiment, ranging from the astrophysical and nuclear interest to the production technique. The experiments aimed to measure the beta halflives and the neutron emission probability of the neutron-magic ^{129}Ag and in the extension ^{78}Ni. These two isotopes are 20 respectively

14 masses heavier than the heaviest stable isotope of the respective element. Creating and detecting such exotic nuclei is a complicated and time-consuming process, if at all possible.

Experience from earlier experiments in the considered mass regions shows that the standard ion sources at CERN-ISOLDE, surface and hot-plasma ion sources, are not suitable for the ionization of silver and nickel. This is mainly due to the massive isobaric background ionized in these sources. In the case of silver, it is mainly indium and cesium, and for nickel measurements, it consists of copper, zinc and gallium. In order to reduce the background in the halflife measurements they have been detected via beta-delayed neutrons. Beta-delayed neutron emission is a unique process for very neutron-rich isotopes. This gives this type of beta halflife determination a higher degree of selectivity compared with the common method, detecting the emitted electrons directly. However, despite this limitation of the number of contaminants the production could not be expected to be clean enough for the detection of the desired isotopes.

In order to improve this situation further it was decided to develop a laser ion source, LIS, based on chemically selective photo ionization. The ionization takes place in a thin capillary attached to the target container. The atoms diffuse out of the target and into this ionizer, where they are ionized by three joined laser beams with well-defined frequencies. Each element has its own unique atomic level scheme which gives this process a chemical selectivity of almost 100%. The laser ionization was made with a pulsed laser system consisting of dye-lasers and high-power copper vapor lasers.

The thesis begins with a short chapter on beta decay and the process of beta-delayed neutron emission. In Chapter 3 the experimental procedure is discussed, where the production and separation at the CERN-ISOLDE facility is presented. Special emphasis is given to the development of the ISOLDE laser ion source, including general aspects of photo ionization in a hot cavity. This chapter also includes a description of the experimental conditions for the two silver experiments, with the common experiment designation IS333, that took place in June 1994 and July 1995 respectively. This contains a discussion of the ionization scheme used for silver as well as a presentation of the detector system and the data acquisition.

Information specifically connected with the nickel production test that took place in September 1994, is treated separately in Chapter 5. The nickel test ran into unexpected production problems, due to extremely long delay times. This makes it a very limited part of this thesis and I have chosen to keep the information connected with it concentrated to one chapter. This is despite the fact that similar aspects of the silver experiments are treated in Chapter 3.

In Chapter 4 the analysis of the experimental neutron data is thoroughly discussed with a general description of the analysis and fit program. The problem of fitting low statistics data is discussed and an evaluation of the biases of chi-square fit methods is made. The results of the halflife analysis of the isotopes $^{120-128}$Ag are presented and the measurements at mass A $= 129$ are discussed.

Finally, I give a summary and interpretation of the results obtained during my thesis work. In the last chapter, some results from some very recent laser ion source tests, made during February and March this year, are presented. This chapter also contains some remarks concerning the future continuation of this work.

Chapter 2

Beta decay

This chapter gives a short overview of beta decay and beta-delayed neutron emission. In Section 2.1 the different types of beta decay, β^+, β^- and electron capture, are presented and their occurrence according to available decay energy is discussed. In the next section the basic theory of beta decay is presented step by step. Owing to this, the $\log ft$ value can be defined as a measure of the transition probability. Selection rules for different degrees of allowed and forbidden transitions together with their $\log ft$ values are presented. The last section in this chapter deals with beta-delayed neutron emission.

In nuclear physics no additional understanding of experimental data is obtained through consideration of the quark model. Many attempts have been made to detect quark effects in nuclear experiments but without success. The nucleon-nucleon interaction can be well described by the exchange of mesons between the nucleons and it is not necessary to consider gluon exchange between quarks.

2.1 Different types of beta decay

Nature always seems to seek the energetically most favourable states. The energy states of atomic nuclei are no exception. One way of decreasing the energy for a nucleus is to undergo decay. The time scale of radioactive decay is determined by the fundamental interaction involved as well as the available decay energy.

A main characteristic of beta decay is that it changes the isospin state of the decaying nucleus with plus or minus one, $\Delta T_z = \pm 1$. The number of nucleons, A, stays constant so that the daughter and granddaughter nuclei are isobars to the mother nucleus. However, sometimes beta decay is *followed* by beta-delayed particle emission which changes A depending on what particles are emitted. The conditions for beta-delayed particle emission are only fulfilled in nuclei far from stability, as will be discussed in Section 2.3.

There are three different types of decay processes classified as beta decay, i.e. electron capture, E.C., beta-plus, β^+, and beta-minus, β^-, decay. When a neighbour in an isobaric chain has a lower energy state it is possible for the nucleus to transform a proton to a neutron or vice versa to pass, in this way, into the lower energy state. To find out if a large enough energy difference exists between two nuclei their masses can be compared.

Let us consider a nucleus $_Z^AX$ and its isobaric neighbour $_{Z+1}^AX$ and their possibilities of undergoing beta decay. Atomic masses, $m(_Z^AX)$ and $m(_{Z+1}^AX)$, will be used in this discussion.

1) In the first case, the mass of $_Z^AX$ is larger than the mass of its isobaric neighbour $_{Z+1}^AX$, $m(_Z^AX) > m(_{Z+1}^AX)$. Thus $_Z^AX$ will decay by β^- decay transforming a neutron to a proton and emitting an electron and an antineutrino.

$$n \rightarrow p^+ + e^- + \bar{\nu} \tag{2.1}$$

2) In this case, the mass of $_Z^AX$ is just a little bit smaller than the mass of $_{Z+1}^AX$, less than two electron masses smaller, $m(_{Z+1}^AX) > m(_Z^AX) > m(_{Z+1}^AX) - 2 \times m_e$. This mass difference is not sufficient for the nucleus to undergo β^+ decay, as this would require that a positron, e^+, is emitted and, in addition, an e^- is absorbed to make a neutral atom $_{Z+1}^AX$. Under these circumstances an electron from the inner orbitals of the electron cloud, from the K or sometimes the L shell, can be absorbed in the nucleus. Thereby a proton is transformed into a neutron and a neutrino is emitted. This process is called electron capture and it is, like β^+ and β^- decay, induced by the weak interaction.

$$p^+ + e^- \rightarrow n + \nu \tag{2.2}$$

3) The last possibility is that the mass of $_Z^AX$ is smaller than the mass of $_{Z+1}^AX$, where the difference is larger than two electron masses, $m(_Z^AX) < m(_{Z+1}^AX) - 2 \times m_e$. In this case $_{Z+1}^AX$ will undergo β^+ decay, transforming a proton to a neutron and emitting a positron and a neutrino.

$$p^+ \rightarrow n + e^+ + \nu \tag{2.3}$$

In beta decay the available decay energy is divided between two particles; therefore, the energy spectra of the electrons are continuous. However, electrons with discrete energy can also be observed in beta spectra. They originate from two totally different processes where none of them has anything to do with beta decay or weak interaction.

When the electron shell is excited, due to an inner electron being captured, for example, the exceeding energy has to be emitted somehow. Normally this is done via photon emission but the energy can also be transmitted to one of the electrons which is then emitted. This process is called the Auger process. The energy of the *Auger electron* is determined by differences in binding energies in the electron shell and is typically of the order of keV.

Similarly, the deexcitation of a nucleus frequently occurs via gamma emission. The excitation energy of a nucleus can also be transmitted to an electron in the shell, however. The energy of these *conversion electrons* are normally higher than for the Auger electrons, of the order of some MeV.

2.2   Beta decay theory for pedestrians

The common understanding of a nucleus today is that it is a bound state of A nucleons, Z protons and N neutrons. Each nucleon is synthesized by three quarks, two *up* and one *down* (*uud*), making a proton, and one *up* and two *down* (*udd*) a neutron. The quarks are kept together in nucleons with the strong nuclear interaction which is described as an exchange of massless vector bosons called gluons. The strong interaction is some 1000 times stronger than the electromagnetic interaction but it has a very short range, of the order of a Fermi, 10^{-15} m.

Beta decay occurs on a long-time scale compared with other processes in a nucleus which are induced by electromagnetic and strong nuclear interaction. This is an indication that the fundamental interaction responsible for beta decay is very much weaker than the electromagnetic and strong interaction. This interaction called the *weak nuclear interaction* has a range of the order of 10^{-18} m. The strength of the fundamental interactions is reflected by the cross-sections for the processes induced by the respective interaction. In this way, it can be seen that the weak interaction is some 10^9 times weaker than the electromagnetic interaction and some 10^{12} times weaker than the strong interaction.

The weak interaction can, in analogy with the strong and electromagnetic interactions, be explained as particle exchange of intermediate vector bosons. The first of these exchange particles, for the weak interaction, was able to be detected at CERN in early 1983. The two $W^{\pm}$ bosons were found to have a mass of 80 GeV and, shortly afterwards, a third boson Z^0 with mass 91 GeV was detected.

However, studying beta decay it is not appropriate to explain, for example, β^- decay in terms of a W^- boson transforming an *up* to a *down* quark, or the e^+ and ν observed in β^+ decay as decay products of a W^+. Instead, this section will have a phenomenological approach taking its starting-point in experimental observables of beta decay. For more complete information about beta decay, see for instance references [Wu66, Seg77].

Starting from Golden Rule Number 2 we get the probability per time unit that an electron with momentum between p and $p + dp$ is emitted,

$$N(p)dp = \frac{2\pi}{\hbar} \langle f|H|i \rangle^2 \frac{dn}{dE_0} \, , \tag{2.4}$$

where dn/dE_0 is the density of possible final states and E_0 is the total available decay energy. The Hamilton-operator matrix element $\langle f|H|i \rangle$ describes the transition between the initial and final state, denoted by indices i and f, respectively.

$$\langle f|H|i \rangle^2 = \int \psi_f^* H \psi_i \equiv |H_{if}|^2 \tag{2.5}$$

Taking a closer look at H_{if}^2, it can be seen that it should contain a measure for the strength of the interaction g and the probability that the two leptons are created in the nucleus. This is represented by the product of the squares of the wave functions, $|\psi_e(0)|^2 |\psi_{\overline{\nu}}(0)|^2$. It also contains a nuclear matrix element describing the possibility of going from the initial state i to the final state f,

$$|H_{if}|^2 = [g|\psi_e(0)||\psi_{\overline{\nu}}(0)||M|]^2 \, , \tag{2.6}$$

where g is a coupling constant describing the strength of the weak interaction. The wave functions $\psi_e(0)$ and $\psi_{\overline{\nu}}(0)$ can be described as plain waves in the form $e^{i\boldsymbol{k}\cdot\boldsymbol{r}}$. These exponential functions can be written as sums,

$$e^{i\boldsymbol{k}\cdot\boldsymbol{r}} = 1 + i\boldsymbol{k}\cdot\boldsymbol{r} - \frac{(\boldsymbol{k}\cdot\boldsymbol{r})^2}{2} + \dots\dots\ . \tag{2.7}$$

The second term in the above sum is small compared to the first which is why it will be neglected. However, it should be noted that we thereby restrict the following to only hold for allowed transitions. The higher order terms lead to forbidden transitions which will be discussed later in this section.

Experiments show that H_{if}^2 consists of a sum of squared nuclear matrix elements with the coupling constants g_V^2 and g_A^2. The indices V and A denote vector coupling and axial-vector coupling, respectively. In vector coupling, the two leptons are emitted with their spins being antiparallel; this transition is called Fermi transition. The axial-vector coupling, on the other hand, corresponds to a transition where the leptons are emitted in a triplet with parallel spins. This is called Gamow-Teller transition.

$$|H_{if}|^2 = g_V^2 M_F^2 + g_A^2 M_{GT}^2 \tag{2.8}$$

To simplify the equations, we will introduce the momentum, η,

$$\eta = \frac{p}{m_0 c} \tag{2.9}$$

and the energy ϵ of the electron in "natural units"

$$\epsilon = \frac{W}{m_0 c^2}\ . \tag{2.10}$$

Further a constant B is defined as

$$B = \frac{2\pi^3 \hbar^7}{m_0^5 c^4}\ . \tag{2.11}$$

Now the probability-per-time unit that an electron with a momentum between η and $\eta + d\eta$ is emitted can be written as

$$
\begin{aligned}
N(\eta)d\eta &= \frac{g_V^2 M_F^2 + g_A^2 M_{GT}^2}{B}\eta^2(\epsilon_0 - \epsilon)^2 d\eta \tag{2.12}\\
&= \frac{g_V^2 M_F^2 + g_A^2 M_{GT}^2}{B}\eta^2(\sqrt{1+\eta_0} - \sqrt{1+\eta})d\eta\ ,
\end{aligned}
$$

or analogously as a function of the energy,

$$N(\epsilon)d\epsilon = \frac{g_V^2 M_F^2 + g_A^2 M_{GT}^2}{B}\epsilon\sqrt{\epsilon^2 - 1}(\epsilon_0 - \epsilon)d\epsilon\ . \tag{2.13}$$

However, up to now the Coulomb interaction has been neglected. The nuclear electric potential influences emitted electrons and positrons differently due to their different electric charges. The positive potential of the nucleus repels positrons, thus giving them

higher velocity than otherwise expected. It has the opposite effect on electrons which are attracted by the nuclear potential and this will reduce their velocity. This effect can be taken into account by the Fermi function, $F(Z, \eta)$, which is a function of momentum, η, and charge, Z. It has been numerically solved and is tabulated. This makes equation (2.12) turn into

$$N(\eta)d\eta = \frac{g_V^2 M_F^2 + g_A^2 M_{GT}^2}{B} F(Z, \eta)\eta^2(\epsilon_0 - \epsilon)^2 d\eta . \qquad (2.14)$$

This is finally the equation which can be used to explain the shape of the energy spectrum of the emitted electrons in beta decay.

2.2.1   Classifications of beta decay

In order to obtain the total decay probability, λ, the integral in equation (2.14) has to range over all momenta or energies,

$$\lambda = \int_0^{\eta_0} N(\eta)d\eta = \int_1^{\epsilon_0} N(\epsilon)d\epsilon = \frac{\ln 2}{t_{1/2}} . \qquad (2.15)$$

To do this, it is appropriate to define a new function, $f(Z, \epsilon_0)$. This function is called the statistical rate function or sometimes the comparative halflife. Tabulated values of $f(Z, \epsilon_0)$ can be found in [Mos51, Fee50], for example.

$$f(Z, \epsilon_0) = \int_0^{\epsilon_0} F(Z, \epsilon)\epsilon\sqrt{\epsilon^2 - 1}(\epsilon_0 - \epsilon)^2 d\epsilon \qquad (2.16)$$

When equations (2.13) and (2.16) are put in equation (2.15) we get a new equation,

$$\int_0^{\epsilon_0} N(\epsilon)d\epsilon = \frac{g_V^2 M_F^2 + g_A^2 M_{GT}^2}{B} f(Z, \epsilon_0) = \frac{\ln 2}{t_{1/2}} . \qquad (2.17)$$

Solving equation (2.17), we can identify the product ft which is a frequently used expression in experimental nuclear physics. It is a measure of the matrix element and coupling constant, as B is a known constant. Experimentally, the determination of the ft value for a beta decay gives information about the corresponding coupling constants. It can be determined for a beta transition by measuring its halflife and maximum energy.

$$f(Z, \epsilon_0) \cdot t_{1/2} \equiv ft = \frac{B \ln 2}{g_V^2 M_F^2 + g_A^2 M_{GT}^2} \qquad (2.18)$$

The function ft is used to classify beta transitions according to their transition probability, or how allowed or forbidden they are. The ft values are extended over a large range which often makes it more convenient to use the logarithm of the ft value, $\log ft$.

The limits of the $\log ft$ values for different types of transitions are not uniquely determined and the $\log ft$ values for different categories may overlap. The used classification

here is widely spread and has been taken from [Wu66]. The group of transitions which is the least hindered and therefore the group of transitions with the shortest halflives (exceptions can occur) is that of the allowed transitions. They can in turn be divided into superallowed and (unfavored) allowed types. Superallowed transitions have a $\log ft < 4$ and they occur mainly for light nuclei, especially in decay between mirror nuclei. Allowed (unfavored) transitions have $\log ft$ values between 4 and 6. All allowed transitions can be recognized by a spin change of the nucleus by one or zero unit of $\hbar$, $\Delta I = 0$, ± 1, and no change in parity, $\Delta \pi = (+)$. We have seen that H_{if}^2 consists of a sum of two different matrix elements, one for Fermi transitions and one for Gamow-Teller transitions. Considering the selection rules, it should once more be noted that there are differences between allowed Fermi transitions, which always have $\Delta I = 0$, and allowed Gamow-Teller transitions which may also change the spin with plus or minus one, $\Delta I = 0$, ± 1. However, Gamow-Teller transitions do not allow $0 \rightarrow 0$ transitions.

The somewhat hindered decays are called first forbidden decays and their spin may also change with $\Delta I = 0, \pm 1$, with the difference, however, that compared to Gamow-Teller decay the parity has to change, $\Delta \pi = (-)$. These transitions have $\log ft$ values between 4 and 6. Unique first forbidden transitions also have a parity change but here $\Delta I = \pm 2$ and their $\log ft$ values lie between 7 and 9. The second and higher-order forbidden transitions are classified in a simular way to the first forbidden ones (see Table 2.1). The halflives and $\log ft$ values in the table have been taken from [Wu66] and have been completed with information from recent Nuclear Data Sheets.

Table 2.1: Classification of beta transitions according to their $\log ft$ values. ΔI in the change of the total spin of the nuclei (+) stands for *no parity change* and (−) for *parity change*.

Transition	ΔI	$\Delta \pi$	$\log ft$	Example	Halflife
Superallowed	$0, \pm 1$	(+)	3.5 ± 0.2	^{1}n	10.3 min
Allowed	$0, \pm 1$	(+)	5.7 ± 1.1	^{35}S	87 d
First forbidden	$0, \pm 1$	(−)	7.5 ± 1.5	^{198}Au	2.7 d
Unique 1st forbidden	± 2	(−)	8.5 ± 0.7	^{91}Y	58.5 d
Second forbidden	± 2	(+)	12.1 ± 1.0	^{137}Cs	30.1 yr
Unique 2nd forbidden	± 3	(+)	11.7 ± 0.9	^{22}Na	2.6 yr
Third forbidden	± 3	(−)	18.2 ± 0.6	^{87}Rb	$4.8 \cdot 10^{10}$ yr
Unique 3rd forbidden	± 4	(−)	15.2	^{40}K	$1.3 \cdot 10^9$ yr
Forth forbidden	± 4	(+)	22.5	^{115}In	$4.4 \cdot 10^{14}$ yr

2.3   Beta-delayed neutron emission

Figure 2.1: Schematic level scheme illustrating one and two neutron emission with separation energies S_n and S_{2n}, respectively.

In isotopes far off stability, beta-delayed particle emission can occur. Several types of particles have been observed during the last years [Jon92], and apart from neutrons and protons also alpha and deuteron emission. Particle emission occurs in nuclei near the driplines with high Q values and low particle-separation energies in the beta decay daughter nuclei.

Beta-delayed neutron emission [Han89] is a unique process for neutron-rich nuclei. Neutron precursors are found all along the nuclear chart for Z in all regions. The most frequently observed neutron emission is the one-neutron emission. However, for nuclei closer to the neutron dripline also more exotic decay channels are possible, such as two- and three-neutron emission. There is even a four-neutron emission branch detected in ^{17}B.

In Figure 2.1, a schematic level scheme for one- and two-neutron emission is shown. A neutron-rich nucleus $_Z^A$X, the so-called precursor, decays by β^- decay to $_{Z+1}^A$X. In case the

decay to the daughter nucleus $^{A}_{Z+1}X$ leads to a highly excited state, where the excitation energy of $^{A}_{Z+1}X$ is higher than the separation energy of one, S_n, respectively two neutrons, S_{2n}, neutrons can be emitted within $10^{-13} - 10^{-16}$ s [Gab87]. This makes it possible to determine the beta halflife of the mother nucleus via the beta-delayed neutrons.

Chapter 3

Experimental procedure

In this chapter the experimental techniques used for the silver experiments are presented. It starts with a general description of the ISOLDE on-line mass separator including the target area and the general purpose separator. The next section, 3.2, treats several aspects of laser ion sources and following that the detection methods for neutrons and betas are described. The chapter ends with some information about the data aquisition, made with the GOOSY system.

Most experiments carried out at ISOL-facilities call for beams with high yields of relatively short-lived isotopes and which are preferably chemically clean. This requires targets with high production yields and fast release in combination with chemically-selective ion sources with high efficiency. The chemical selectivity is especially a condition which causes problems for some elements. Due to this the high production rates cannot always be appreciated as the high background level covers the interesting events.

This was the situation during the earlier attempt to reach the neutron-rich silver isotopes dealt with in this thesis. The isobaric background from indium in particular made it impossible to get any information on the silver isotopes. This was the motivation for the decision to develop a laser ion source for CERN-ISOLDE for the ionization of silver.

3.1 CERN-ISOLDE

The silver and nickel experiments described in this thesis were carried out at the "new" on-line isotope separator ISOLDE at the CERN PS-Booster facility, PSB, in Geneva. Formerly, ISOLDE was located at the CERN proton syncro-cyclotron, SC. However, as the SC was closed down after 33 years of operation in December 1990, it was decided that the existing physics program at ISOLDE should be maintained as a part of the scientific program at CERN for the future. To be able to do so, a suitable new site had to be found for the separator. The solution was to integrate ISOLDE in the CERN PS-accelerator complex and connect the separator with the PS-Booster.

The PS-Booster is a different type of accelerator than the SC was. Here, the protons are pre-accelerated by a linac and then injected into the stack of four small synchrotrons which make up the PSB. From there, the 1 GeV protons are further distributed to the high-energy accelerators at CERN, as well as to ISOLDE. This proton beam differs in
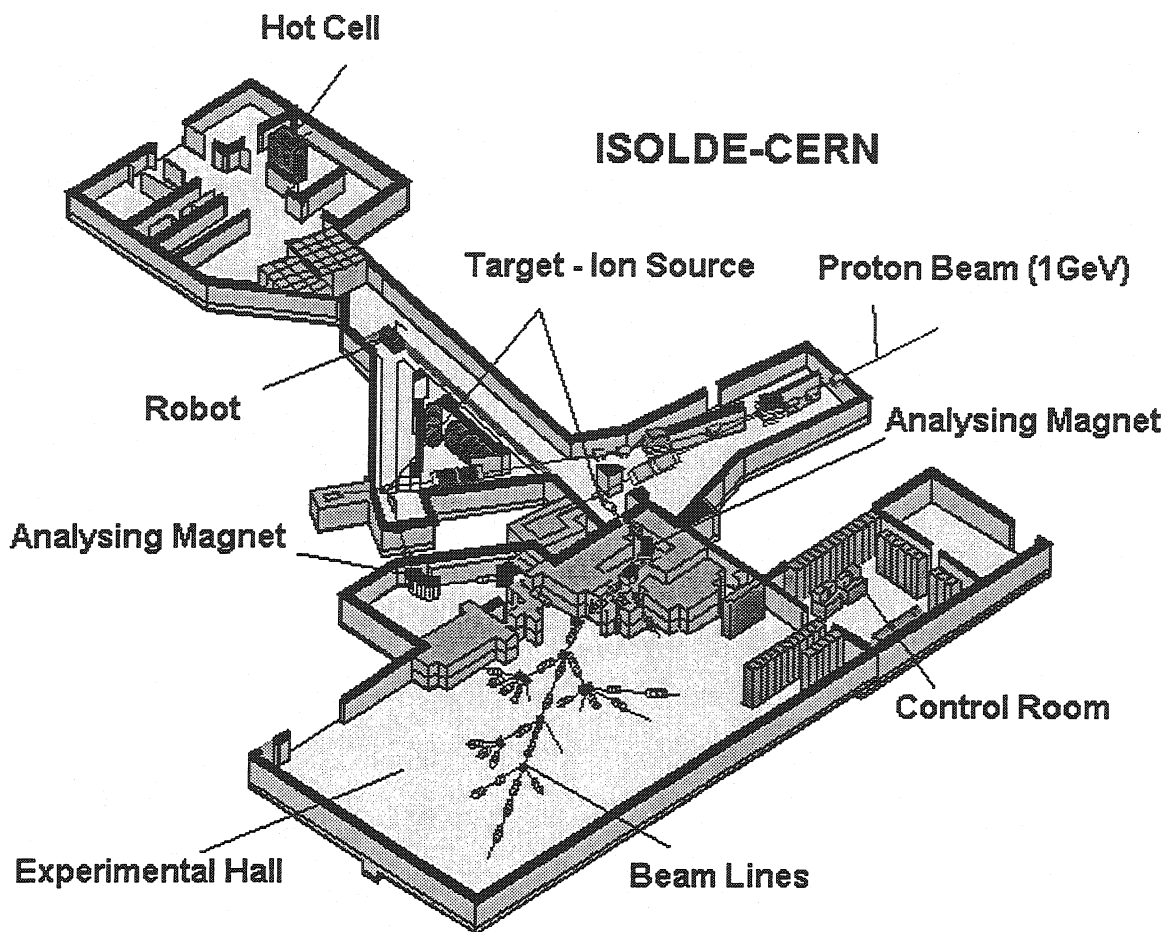
Figure 3.1: A view of the new ISOLDE PS-Booster facility at CERN. The whole area shown in the figure, except the experimental hall: is up to 8 m below ground level.

several ways from the beam ISOLDE was provided with by the SC. Primarily the energy has increased from 600 MeV to 1 GeV. However, also the time structure has changed from a continuous beam to a high-intensity pulsed beam with low repetition rate. The operation of the PSB is divided into supercycles. They normally contain 12 equidistant proton pulses and have a total length of 14.2 s. However, due to development work for a heavy-ion program at the PS the supercycles have recently been extended, to 16 pulses and 19 s, for some periods. The proton pulses are very short (only 2.4 μs) and they may reach intensities of $3 \cdot 10^{13}$ protons per pulse (see Table 3.1).

Figure 3.1 shows an overview picture of the ISOLDE-PSB facility which has been in operation since 1992. The ISOLDE facility consists of several parts, the front end being where the radioactive isotopes are produced in a fixed target. Directly attached to the target is the ion source from which the ions are electrostatically accelerated into the separator. Connected with the separator is a beam distribution system through which all experimental positions can be reached. In this section only the production in the target and the mass separation is discussed. The development of the ionizer is an essential and major part of the preparations for the described experiments, so this is separately treated in Section 3.2.

Table 3.1: Beam parameters for the CERN PS-Booster proton accelerator.

Beam energy	1 GeV
Maximum intensity on target	$3.2 \cdot 10^{13}$ p$^+$/pulse
Pulse length	2.4 μs
Repetition time	1.2 s

3.1.1   Production and isobaric contamination

The proton beam is transferred from the PSB through an underground tunnel to the ISOLDE target area, some 100 meters away. There the protons hit a fixed target which also acts as catcher for the beam, thermalizing the radioactivity. The target area is divided into two separate target positions, one for the general purpose separator, GPS, and one for the high resolution separator, HRS. The two target positions are designed with the options to be operated in beam-sharing mode.

The production of radioactive isotopes at ISOLDE is made by means of proton induced fission or spallation. The created fission products evaporate out of the target as atoms and diffuse from the target container into the attached ion source; see Figure 3.4 in Section 3.2.3. Protons of energy 1 GeV have a very high penetrability which makes it possible to work with thick targets containing high amounts of target material. In this way high production rates can be obtained.

The main requirements for target material are that it should have a high production cross-section and a fast release for the isotopes one wishes to investigate. It must also be chemically stable and not have an aggressive influence on the target container. The most widely-used targets at ISOLDE are thick uranium carbide, UC_2-C, targets in combination with surface ionizers. However, also silicon and thorium carbide are used as well as foil targets of different material, for example Nb, Ta and Ti. Recently, the first molten liquid targets have been used for experiments at ISOLDE-PSB, after some additional problems due to the high-intensity pulsed beam from the PSB. The list of available targets at ISOLDE is long and the ones mentioned here are just a few examples. For more information, see references [Rav79, Hag92]. To simplify the off-line tuning of the mass separator a *mass marker* is sometimes added to the target. This is a stable isotope which evaporates out of the target even at the low temperatures applied for the out-gasing.

Most targets are kept in cylindrical containers made of tantalum, with a typical length of 20 cm and a diameter of 20 mm. The target container is resistantly heated and in addition the proton beam contributes with a non-negligible temperature increase.

In the two silver experiments thick uranium carbide targets were used. In the first experiment, in June 1994, the target had a thickness of 11 g/cm^2 which was increased to 44 g/cm^2 for the next experiment in July 1995. For silver, the maximum production rates obtained with proton-induced fission lie at somewhat lighter masses than for indium.

As a consequence, the yields for the neutron-rich indium isobars are some two orders of magnitude higher than for silver. In addition the ionization potential for indium, IP = 5.8 eV, is much lower than for silver, IP = 7.6 eV [Nor80]. The low IP of indium makes it a suitable element for surface ionization. Unfortunately, this feature also makes it an element which is very difficult to resist ionization in a hot cavity.

3.1.2 General purpose separator

When the ions leave the ion source they are electrostatically accelerated with 60 kV. Due to the pulsed proton beam, intense ionization of air is produced in the beam path both in front of and behind the target. The normal state-of-the-art procedure would be to keep the target and ion source at high-voltage compared to their surrounding. However, a high-voltage supply might not survive these intense ion pulses for a very long time. In order to avoid this problem a pulsed high-voltage supply was installed which brings down the high-voltage from 60 kV to 0 within 35 μs. This is done before the proton beam hits the target and afterwards the pulse is brought back up to its original value within 10 – 20 ms [Kug92]. It is also possible to use the high-voltage supply in a continues mode for off-line stable-beam experiments.

The mass separation was made with the ISOLDE general purpose separator, GPS, which has a mass-resolving power of 2400. The mass-over-charge selecting magnet has a bending radius of 1500 mm and a bending angle of 70°. In addition, a system of focusing quadrupoles, bending magnets and kickers is used to bring the ions to the selected experimental site with the highest possible transmission. Neutron detection is normally made at the experimental point LA1, as this is the most favourable position considering the neutron background from the beam impact. This beamline has the advantage that with this central-mass beam it is possible to simultaneously take out one high- and one low-mass beam with mass differences of ± 3 – 15% respectively, from the central mass. This was used in the second part of the silver experiment to perform gamma spectroscopy on ^{124}Ag in parallel with neutron measurements on $^{128-129}$Ag.

3.2 Laser ion source

There have been earlier experiments made on neutron-rich elements in the $A = 130$ region with different types of ion sources at CERN-ISOLDE. They have shown that neither surface ion sources nor plasma ion sources are suitable for ionizing neutron-rich silver isotopes. The surface ion sources are not sufficient due to the relatively high IP = 7.6 eV of silver. Plasma ion sources do ionize silver, but not only silver; they ionize basically all elements produced in the mass region. This gives rise to a very high isobaric background. It was clear that if one wanted to detect neutron-rich silver at ISOLDE a chemically selective method had to be found.

The choice of method for this project fell to a laser ion source, LIS. In this section the principles behind a LIS are discussed and the developed construction is presented. The

section starts with some general aspects of ionization in a hot cavity, such as surface ionization in Section 3.2.1 and the function of a thermal plasma in an ionizer. In the next section, 3.2.2, the basis for a LIS, i.e. resonance laser ionization, is discussed and the ionization scheme used for the silver experiments is presented. The design of the ionizer and the laser setup which was used are shown in Section 3.2.3 and 3.2.4 respectively.

3.2.1   Ionization in a hot cavity

Before going into the details of photo ionization, surface ionization and the role of a thermal plasma in a hot cavity is considered. These processes are of interest also in a LIS as the surface ionization of elements with low IP, for example indium, cannot be avoided. Independent of their origin, all ions are influenced by the ion accumulation effect present in hot cavities due to the thermal plasma.

Surface ionization is well known and is frequently used for ion source applications. When an atom hits a wall it may lose or gain an electron. The surface ionization degree α and the surface ionization efficiency β for these processes can be calculated with the Langmuir equation,

$$\alpha = \frac{n_i}{n_0} = (\sigma_i/\sigma_0)\exp[(\varphi - W_i)/kT] \tag{3.1}$$

$$\beta = \frac{n_i}{n_i + n_0} = \frac{\alpha}{1 + \alpha} \, .$$

The Langmuir equation is applicable for both positive and negative surface ionization for details see [Kir81]. The indices i and 0 denote ions and atoms respectively. Furthermore, n is the number density, σ statistical weights of atomic or ionic ground states, φ the work function of the surface material and W_i the ionization potential of the atoms.

However, it has been experimentally found that the ionization efficiency of hot cavities is very much larger than for surface ionization. This is a puzzling fact, especially when surface ionization is the sole ionization process. The answer to this riddle is that the recombination is inhibited by the creation of a thermal plasma inside a hot cavity. The plasma is generated through a flux of glow electrons and surface ionized ions from the wall into the volume. This distribution of electrical charge gives rise to an attractive potential trough along the axis of the capillary and a repelling potential along the walls for the positive ions. When the atoms have been ionized, in a wall collision or with photo ionization, they are trapped in the plasma if they do not have too high a kinetic energy. Once they are trapped in the potential trough the probability of recombination becomes very small. Due to this effect, the ionization efficiencies for trace elements in hot cavities exceed by orders of magnitude the one for surface ionization. The ionization efficiency, η, for a hot cavity assumed to be in thermal equilibrium is in the ideal case described by the Saha equation [Kir78]

$$\frac{\eta^2}{1 - \eta^2} = 2\left(\frac{2\pi m}{h^2}\right)^{3/2} P^{-1}(kT)^{5/2}\exp(-W_i^*/kT) \, , \tag{3.2}$$

when only one element, with an ionization potential of W_i^*, is present in the cavity. $P = kT(n_0 + n_i + n_e)$ is the plasma pressure. Thermo ionization in hot cavities, which

has been discussed here, has been discussed in detail in several publications. For more information on this subject see references [Kir81, Huy83, Kir90, Dup92].

As a consequence of the above, we see that surface ionization in a LIS is on the one hand a desirable process, as it contributes to creating a thermal plasma which acts as an ion trap and increases the ionization efficiency. On the other hand, it is an unwanted process as it can ionize atoms of undesired elements. The condition for such isobaric contaminations is that there are neighbouring elements, with low IP, produced in considerable amounts compared to the desired isotopes. This condition is unfortunately very well fulfilled for measurements of neutron-rich silver. There are two elements which are produced with comparable or even higher yields in proton-induced fission than silver. The element with the lowest IP of 3.9 eV in the whole periodic table is cesium. This makes it almost impossible to avoid as an source of isobaric contamination in this mass region. Fortunately for the silver measurements the problematic cesium isobars lie on the other side of the beta-stability line and do not emit neutrons. However, the beta measurements are very much disturbed by the Cs isotopes. The other contaminant, indium is with its IP of 5.6 eV another candidate for surface ionization. Indium has only two protons more than silver and therefore the mass region where isotopes of both elements emit beta-delayed neutrons overlap, starting at $A = 127$.

3.2.2   Resonance laser ionization

The LIS applied at CERN-ISOLDE is based on resonance laser ionization. This type of ionization is of non-thermal nature and is based on that the atoms are excited and ionized by laser light when the frequencies coincide with the atomic transitions. Each element has its own unique electron shell structure; which gives resonance laser ionization a very high chemical selectivity of nearly 100%. A further advantage is that photo ionization is a process with high efficiency, it may reach tens of percent. Resonance photo ionization in a LIS using copper vapour lasers, CVLs, has been described in details in reference [Mis93].

In the initial state of the LIS development for Ag different types of ionization processes were considered. These are schematically represented in Figure 3.2. The work with the laser ionization for Ag has been described in details in reference [Sch93]. The ground state of Ag is at typical LIS operation temperatures (2000 - 2500 K), thermally populated to almost 100%. From the 5s $^2S_{1/2}$ ground state the first transition goes to the 5p $^2P_{3/2}$ state. There is only the 5p $^2P_{1/2}$ state between them to which no spontaneous decay can take place. This fact excludes losses which could arise from that the atoms are pumped away into some undesirable, third state. Thus, an atom decaying from the second state can only end up in the ground state. There it has a new chance of being excited by the laser light. The second transition can be chosen in several ways. The choice is influenced by the parity and spin of the involved states; as well as the ionization process applied. The ionization can be made by different means. It is possible to resonantly excite Rydberg states, which lie close to the ionization potential. From a Rydberg state the atoms can either be ionized by a high-voltage electrical field or via particle collisions. An other possibility is to use an auto ionizing state[1], AIS, when one with suitable
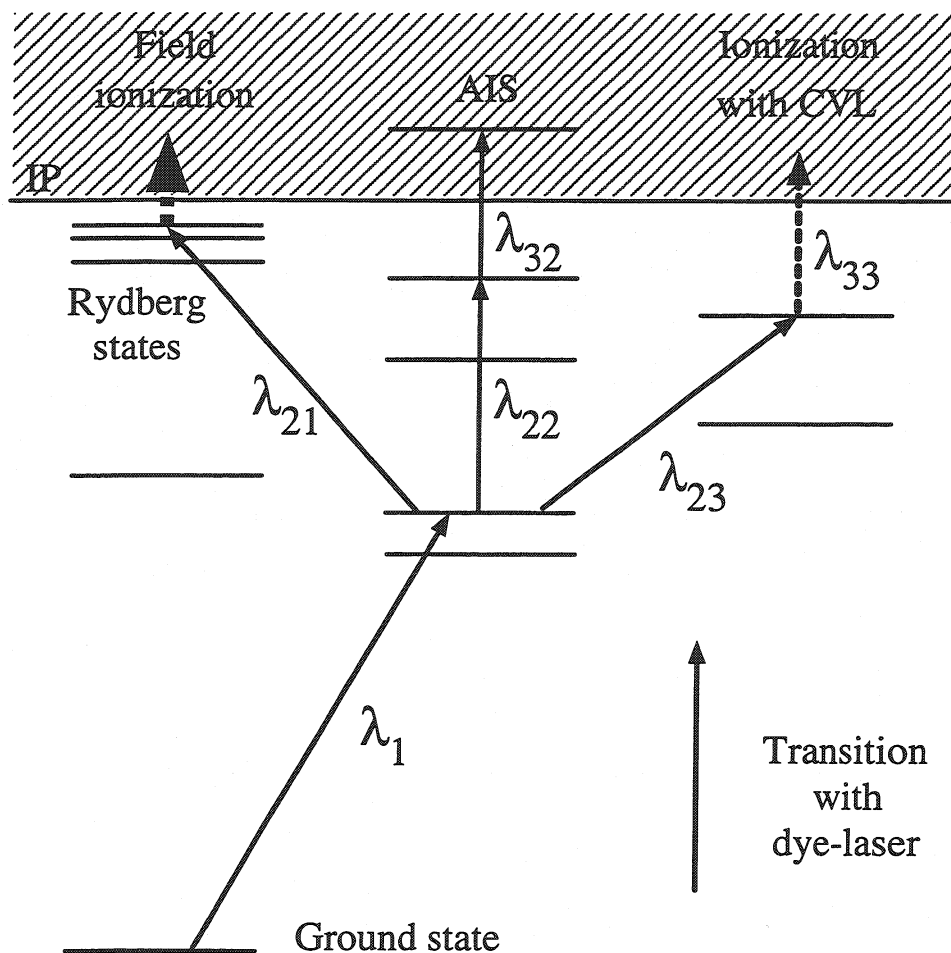
---

[1]A bound two-electron excitation above the IP.

Figure 3.2: Schematic picture of resonant ionization. The first transition, λ_1, is common for all three options; λ_{21} goes to a Rydberg state from which the atom is ionized with an electric field. The second option goes via λ_{22}, and λ_{32} to an auto ionizing state. Option number three is similar to option two, with the only difference that the ionization, λ_{33}, is non-resonant into the continuum with a beam from a copper vapour laser, CVL.

properties exists. With an AIS the cross-section for the ionization can be increased up to 10^{-14} cm^2 which should be compared to the cross-sections for non-resonant ionization into the continuum which is of the order of 10^{-17} cm^2 [Sch93]. However, measurements described in the earlier reference has shown that no suitable AIS could be efficiently excited in silver. The third possibility is to ionize the atoms into the continuum by brute force. Due to the low cross-sections of non-resonant ionization a powerful laser is needed for this type of ionization; which is the reason for that a copper vapour laser is well suited.

Off-line measurements have shown that the most efficient alternative for a LIS for ionization of silver was non-resonant photo ionization, using a CVL for the third transition, see Figure 3.3. The resonant excitation of the first atomic transition was made from the ground state (5s ^{2}S$_{1/2}$ $\longrightarrow$ 5p ^{2}P$_{3/2}$) with $\lambda_1 = 328.07$ nm and the second transition (5p ^{2}P$_{3/2}$ $\longrightarrow$ 5d ^{2}D$_{5/2}$) with $\lambda_2 = 546.55$ nm using tunable dye-lasers pumped by copper vapour lasers. Both these transitions have the advantage that there are no intermediate levels to which the atoms spontaneously can decay. As has been discussed earlier this fact prevents losses. The two resonant transitions were deeply saturated with laser power of

$P_1 = 5$ mW and $P_2 = 400$ mW [Fed95].

The cross-sections of resonant optical excitations are determined by $\sigma_0 = \lambda^2/2\pi$. This is true under condition that; *i)* the light is monochromatic, i.e. the laser linewidth is smaller than the natural linewidth, and *ii)* that there is no inhomogeneous broadening, i.e. Doppler broadening. In the present case, the spectral width is larger than the Doppler width. Then σ_0 has to be reduced by a factor $\Delta\nu_{natural}/\Delta\nu_{laser}$. Taking the first transition λ_1 as an example, it has a transition probability A of $1.4 \cdot 10^8$ s^{-1} [Wie80]. This gives the transition a natural linewidth of $\delta\nu = A/2\pi = 2.2 \cdot 10^7$ s^{-1} = 22 MHz. The width of the dye-laser used in the first transition is 6 – 10 GHz, however, due to frequency doubling the linewidth is increased with a factor of 1.5 – 2. For the first transition this gives a cross-section of $(328 \cdot 10^{-7}$ cm$)^2/(2\pi) \cdot 22$ MHz/20 GHz $\approx 2 \cdot 10^{-13}$ cm^2. However, the excitation efficiency is not exclusively determined by the cross-section. It also depends on the available laser power and the pulse repetition rate of the laser compared to the lifetime of the levels involved. As a consequence, the second-step excitation has to be faster than the decay back to the ground state.

The non-resonant ionization step could not be saturated. In the first beamtime 2.5 W could be focused into the ionizer. This only represented a tenth of the available laser power. For the second beamtime this figure was increased to about 7 W, with a corresponding increase in the ionization efficiency. The off-line photo ionization efficiency of silver for the Nb ionizer was determined to 10.8%. This should be compared to the surface ionization efficiency of indium which was of the order of 0.7%. Tests of improved ionizer constructions took place during the final stage of the work with this thesis. Due to this fact the results from those tests were not integrated in this chapter but has been separately reported on in Chapter 7.

The isotope shift between ^{107}Ag and ^{109}Ag has been measured to 450 MHz (see reference [Fis75] and further references in that publication). The isotope shift do in the worst case progress linearly with the mass, which gives a maximum isotope shift of some 5 GHz from ^{107}Ag to ^{129}Ag. With a laser linewidth of 12 – 20 GHz this effect can be neglected.

Another effect which could give rise to complications is the hyperfine structure. Measurements on light silver isotopes have shown that the hyperfine interaction is extremely dependent on the spin of the nuclear ground state [Ful69]. For $^{105-113}$Ag a level splitting of 1.5 – 2.5 GHz has been measured for the atomic $^2S_{1/2}$ ground state. These isotopes all have spin $1/2^-$. However, for ^{103}Ag the situation is dramatically different. This isotope has a spin of $7/2^+$ and a hyperfine splitting of 39.7 GHz. Measurements on indium isotopes show that the situation is equally bad or even worse with a spin of $9/2^+$. A simple calculation shows that: if the hyperfine splitting for ^{103}Ag is $\Delta W = 40$ GHz $\propto$ $(I + 1/2) \cdot \mu_I/I$ with a $7/2^+$ and $\mu_I \approx 4$ [Rag89]. Measurements of indium isotopes with $9/2^+$ ground states have given $\mu_I \approx 5.5$. This is also a resonable approximation for silver isotopes with the same ground states configuration. Then the hyperfine splitting should be of the order of $1.3 \cdot 40$ GHz = 53 GHz in a silver isotope with a $9/2^+$ ground state. Such a large shift of the ground state could lead to that the laser light would no longer be able to excite the first excitation or only do it very inefficiently. Furthermore, one could also expect losses due to optical pumping into non-desirable states.
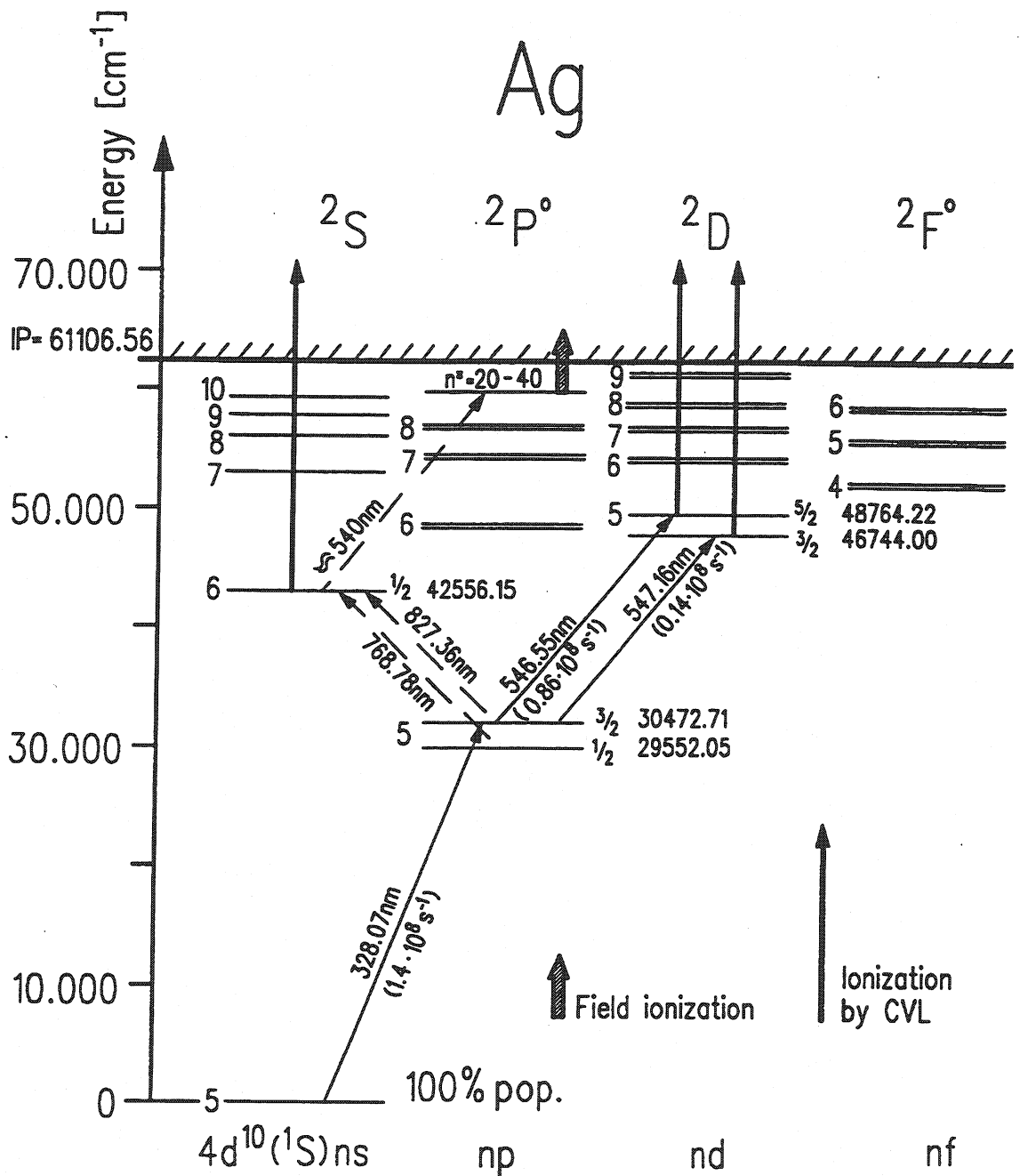
Figure 3.3: A selected part of the atomic level scheme for silver, taken from reference [Sch93]. Different transitions investigated in the development phase of the LIS for silver are indicated. Among those, also the ionization used during the experiments with $\lambda_1 = 328.07$ nm, $\lambda_2 = 546.55$ nm and the non-resonant ionization, into the continuum, with a CVL is shown.
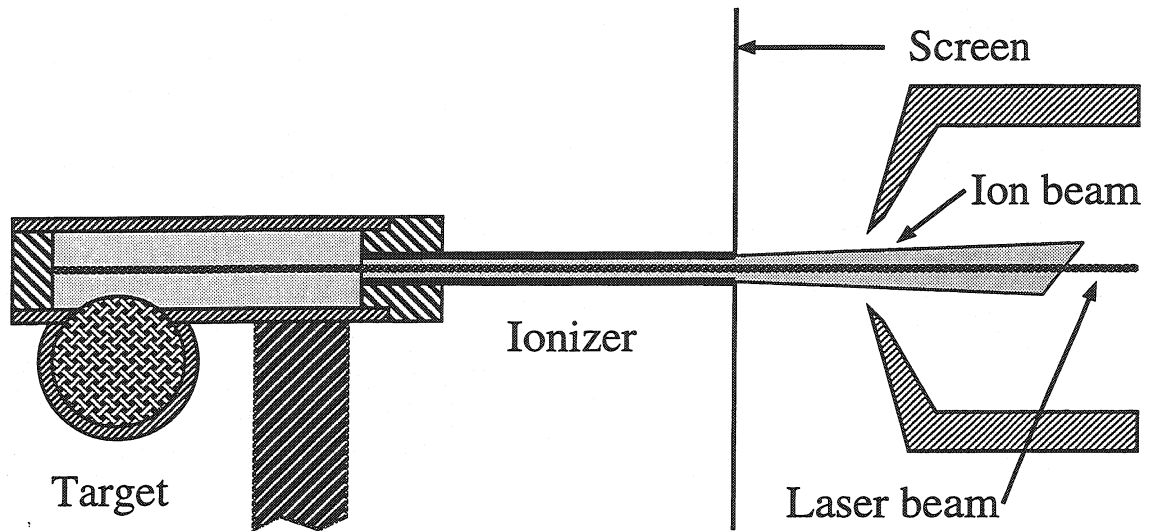
3.2.3   Design of the ion source

Figure 3.4: Schematic view of the target and ionizer used for the experiments. The atoms diffuse out of the target chamber into the ionizer where they are ionized by the laser light.

The ionizer used for the latest silver beamtime consisted of a 30 mm long niobium tube with an inner diameter of 3 mm and an outer diameter of 5 mm (see Figure 3.4). It was resistantly heated, independent from the target, to working temperatures of some 2000 to 2200 K. The construction of the LIS at ISOLDE is based on the long experience with the surface ionizers and the mechanical construction has been taken over without big changes. To design the ionizer as a capillary with diameter $\ll$ length, where the diameter is of the order of the laser beam diameter has proven to be a very efficient shape compared with other tested geometries [Mis93]. To efficiently extract ions out of a capillary, an electric potential drop is applied over the length of the capillary. For the metal capillaries tested this potential was of the order of one volt.

The selectivity and efficiency using the different wall materials Ta, Nb and Ta-C have been tested on- and off-line [Mis93]. Based on these tests it was decided to use a niobium cavity for the first on-line silver experiments with the LIS.

The niobium cavity used during the first beamtime had a slightly smaller diameter, with thinner walls than the one described above. This resulted in a mechanical instability which made the tube bend at high temperatures. As a consequence the laser light could only reach part of the ionizer volume which, as expected, decreased the photo ionization efficiency drastically. This problem was prevented in the later experiment through a mechanically more stable construction as well as a somewhat lower working temperature.

Microgating

The surface ionized indium isobar is still the limiting factor for the identification of ^{129}Ag. In order to further decrease this type of contamination a microgating is being developed.

The surface ionization and release of indium is constant in time between the laser pulses. During the proton pulse the high voltage for ion extraction is switched off, as has been discussed in Section 3.1.1. The time of the laser ionization is limited to 20 ns. However, the duration of the photo ion pulse is determined by the extraction of the ions from the cavity. With a voltage drop of some volts it was in the order of 30 μs. Assuming that 90% of the silver ions have left the ionizer within 50 μs after the laser pulse, the beamgate could be closed for the next 50 μs, until the next laser pulse comes. This way one would reduce the indium by 50% at the price of loosing 10% of the silver ions. The sharper the silver ion pulse can be made, the higher the selectivity one can obtain.

On-line tests with microgating for the niobium ionizers, in connection with the silver experiments, did, however, not give satisfying results. The losses of silver compared with the gain in selectivity were considered to be too large with the obtained time structure. To improve the time structure a ceramic cavity of sapphire with a higher voltage drop of 20 V over the capillary has been tested off-line. To heat the sapphire capillary a graphite tube with a somewhat larger diameter was placed around it. In order to get as high a resistance as possible, cuts were made in the external graphite tube. Sapphire is a rather brittle material which makes it difficult to tool and install this type of ionizer. However, up to now one off-line test has been made with a sapphire ionizer and the ion pulse showed a very nice time structure. Unfortunately, the ionization efficiency was measured to only 1 per mille compared with 10% off-line for the niobium catcher. Nevertheless, further tests are planned for the ceramic ionizer and development work is being continued to improve the construction (see Chapter 7).

3.2.4   The laser setup

During the experiment, as well as in the preparation phase in Mainz, high-power copper vapour lasers in combination with dye-lasers were used. A high repetition rate in combination with high power make CVLs especially suitable for LIS applications at ISOL-facilities, where the efficiency is a very critical factor.

In the test phase in Mainz, commercially available CVLs from Oxford Lasers were used in combination with dye-lasers from Lambda Physik. For the experiments at ISOLDE, Russian-produced CVLs with a repetition rate of 10 kHz were used in combination with dye-lasers developed at the Institute of Spectroscopy, ISAN, in Troitsk. All lasers mentioned here have been described in detail in Chapter 5.2 in [Sch93]. The three CVLs can be used to pump three dye-lasers tuned to resonance with the desired transition. The first transition was ultraviolet in the cases of Ag and Ni and is thus more energetic than the two frequencies of the CVL beam, $\lambda_{yellow} = 578.21$ nm and $\lambda_{green} = 510.55$ nm. This makes it necessary to use dye-laser frequency doubling to reach the wavelength of interest. This is done with a non-linear barium-beta-borate, BBO, crystal. A schematic picture of the laser setup for the silver experiment is shown in Figure 3.5.

In order to have access to the lasers for calibration and maintenance during the beamtime the laser system at ISOLDE is situated about 20 meters from the target and the ion
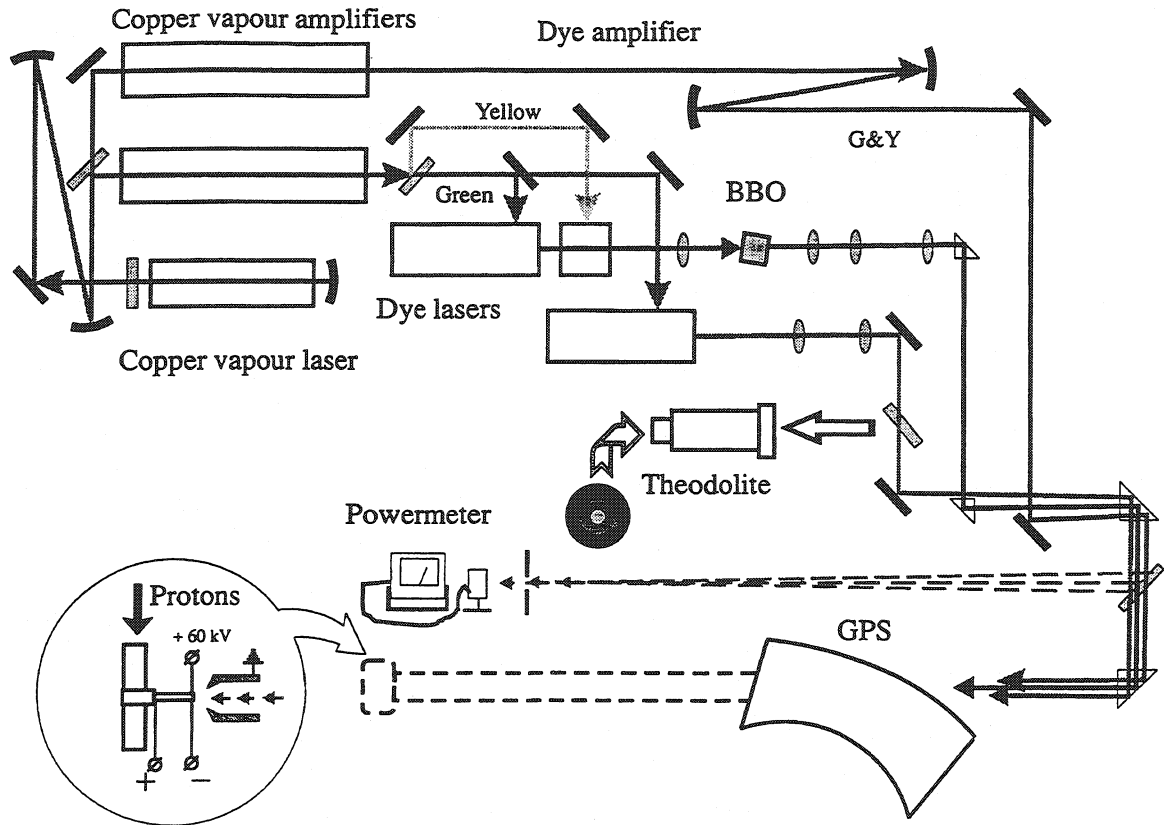
Figure 3.5: Schematic view of the laser setup used at ISOLDE.

source. To be able to focus three beams of different wavelengths over this distance, it was necessary to apply one two-lense telescopes to the dye-laser beams and a spherical mirror telescope to the CVL beam. The last six meters before the ion source the laser beams are sent through a channel in the separator magnet. This makes it impossible to introduce any optical elements into the beam over this distance. In order to focus the highest possible fraction of the beam in the laser ion source it is necessary to work with low-divergency beams. This is a problem with CVLs as they generally deliver very high-divergency beams. To improve the divergency, one CVL functioning as as oscillator was equipped with an unstable resonator. The beam of the oscillator was divided and sent into two other CVL amplifiers. In this way the divergency of the beams from the amplifiers is determined by the reduced divergency of the oscillator.

In the first experiment, the stability of the laser frequencies were checked by observing the photo ion current of stable silver in a Faraday cup. A separate oven with stable silver was placed under the target container with a special inlet to the target chamber. For the second experiment, already the yields of the radioactive long-lived [111]Ag were high enough to be observed in the Faraday cup. This made it possible to abolish the construction with the oven.

3.3 Detection

Some neutron-rich isotopes have the feature that a certain percentage of the nuclei emit neutrons after beta decay, so-called beta-delayed neutrons. As the neutron emission comes promptly, within some 10^{-13} to 10^{-16} s after the beta decay, it can be used to determine the β—halflife. Since only neutron-rich isotopes emit beta-delayed neutrons, it is possible in certain isospin regions to get a high selectivity and background suppression through the use of neutron detection for halflife determination instead of detecting the beta decay directly. This is the case with the silver isotopes $^{120-126}$Ag, for example, as the indium isobars do not yet emit neutrons.
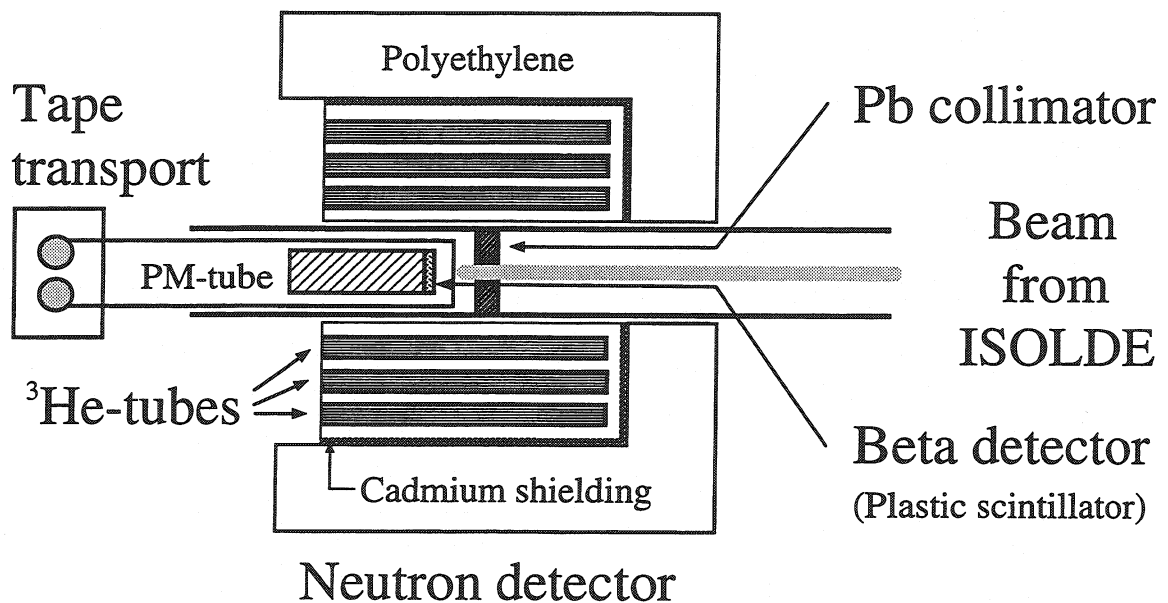

Figure 3.6: Detector setup with the beta-scintillator detector positioned behind the tape in the center of the neutron-long counter.

The detector setup consisted of a cylindrical neutron detector covering almost 4π, through which a beam pipe from the separator is brought. In the middle of the detector a lead collimator is placed with an axial hole of 3 mm in diameter. Behind the collimator, a beta detector is positioned and between the collimator and the beta detector a tape is mounted to avoid accumulation of long-lived activity in front of the detector. The tape was moved once per supercycle to keep down the beta background, mainly from isobaric cesium. The detector setup is shown in Figure 3.6. Standard NIM electronics were used including preamplifiers and amplifiers for the detectors.

3.3.1 Neutron detection

Neutral particles cannot be detected directly; this has to be done indirectly via a charged reaction partner which in turn can be detected through Coulomb interaction. The neutron detector used in these experiments consists of three concentric rings with in total

50 cylindrical chambers filled with ^{3}He gas. The commonly used reaction for neutron detection ^{3}He$(n,p^+)^3$H has a Q-value of 764 keV and a cross-section for thermal neutrons of $\sigma_{th} = 5.33 \cdot 10^3$ barn. The cross sections for more energetic neutrons are some 3 orders of magnitudes lower which makes it very important to moderate the neutrons before detection to keep the efficiency high. This is most efficiently done through collisions with particles with a mass close to the neutron mass. To achieve this, the gas chambers are embedded in a matrix of polyethylene. Outside the outer detector ring a cadmium box is placed to absorb the background neutrons from the outside; those are also moderated to reach higher absorbtion in the cadmium plate. For more detailed information on this kind of detectors, see references [Ohm81, Ten88].

3.3.2   Beta detection

It was planned to use beta detection for determining the beta-delayed neutron probability, P_n. A hardware coincidence gate was set for β-neutron coincidences. However, the nuclei of interest lay up to 7 masses away from stability and some of the isobaric contamination is produced with orders of magnitudes higher rates than the interesting silver isotopes. This makes the random coincidences too frequent, so it is impossible to use this method. The best method is probably to take the data in list mode and, by means of software, to set the gates off-line. With this method it might be possible to get a true β-neutron coincidence spectrum but it is in any case difficult to filter out the interesting beta decays from the mass of beta decays. This is also needed to derive a P_n value.

The beta detector consisted of a 1 mm thick scintillator disc with a diameter of 19 mm placed on a photomultiplier. The dimensions are so small in order to fit inside the beam tube going axially through the neutron detector.

3.4   Data acquisition

The data acquisition was made with the GOOSY system provided by the ISOLDE-collaboration and the data were taken with multi-stop CAMAC time-to-digital converter modules, TDCs. One TDC was connected to each neutron detector ring and one for the beta detector. The spectra from the TDCs went into histogramming memory modules and were saved in the ISOLDE-VAX computer. GOOSY is developed at GSI, Darmstadt, and is the standard acquisition system at CERN-ISOLDE.

The data were taken as singles spectra, meaning that each spectrum was opened and closed for several measuring cycles. The data points coming from the different measuring cycles cannot be identified as belonging to a special cycle, in contrast to list mode data. The data were taken with 1 or 2 ms channels in either 1 K, 1024 channel or 4 K, 4096 channel spectra. All spectra were started with the so-called T_2 signal. It is sent out from the electronics of the accelerator when the 60 kV extraction voltage is back up to its full value after a proton pulse. After a preset time, a beamgate is closed and remains closed until the next proton pulse and measuring cycle.

3.5   Summary of experimental conditions

Silver experiment, IS333 – June 1994

Number of shifts:		14
Available pulses/supercycle:		max. 5
Target:	Material:	uranium carbide cloth, UC_2-C
	Thickness:	11 g/cm^2
Ion source:	Material:	niobium
	Length:	30 mm
	Inner diameter:	2 mm
	Outer diameter:	3 mm
Microgating:		not applied

External oven with Ag stable mass marker

Silver experiment, IS333 – July 1995

Number of shifts:		27
Available pulses/supercycle:		max. 8
Target:	Material:	uranium carbide cloth, UC_2-C
	Thickness:	44 g/cm^2
Ion source:	Material:	niobium
	Length:	30 mm
	Inner diameter:	3 mm
	Outer diameter:	5 mm
Microgating:		not applied

Chapter 4

Analysis of $^{120-128}$Ag halflives

This chapter starts with a brief presentation of the statistics for measured count numbers. In Section 4.1 the fit program used, MINUIT, and the MINOS errors are presented and the different properties of the maximum likelihood and χ^2 fit methods, especially at low statistics, are discussed (based on publication [Jad96]). Section 4.2 treats the actual theoretical models to which the data are fitted and discusses complications through isomers. In Section 4.3, the background and the halflives measured with beta-delayed neutrons for $^{120-128}$Ag are presented as well as measurements at mass 129. This last section also contains an estimate of the production rate of the measured isotopes at ISOLDE.

To get information about physical properties, experimental methods delivering count numbers as an output are often applied. Consequently, an essential problem in data analysis is to fit count numbers. In order to obtain useful and correct information about the physics one wishes to study, it is necessary to know that the counts, n_i, are Poisson distributed [Hai67, Joh92],

$$P(n|\mu) = \mu^n e^{-\mu}/n! . \tag{4.1}$$

The total number of channels is denoted by N_0, and μ is the "true" value. The outcome of the analysis is the estimates θ_i for the values μ_i. For large count numbers a Poisson distribution converges to a normal distribution

$$P(n|\mu) = \frac{1}{\sigma\sqrt{2\pi}} \exp\left(-\frac{(n-\mu)^2}{2\sigma^2}\right) \tag{4.2}$$

where σ^2 is the variance of the distribution. The fit methods that maximize the likelihood functions are based on that the data are Poisson distributed whereas χ^2 methods presume normal distributed data. For high statistics these two methods are equal and both methods deliver reliable results. However, when applied to Poisson distributed data one has to be aware that non-physical effects can occur due to existing biases in the χ^2 methods (see Section 4.1.2).

Before going into the details of the analysis, a more exact description will be made of what the concept "to fit" means. Three different steps can be identified, namely a goodness-of-fit test (called "test of hypothesis" in statistics), the determination of a parameter value ("point estimation") and a determination of the error bars on the parameter ("interval estimation"). Although there exist methods which can be used to obtain results for all three steps, one must keep in mind that they are principally different.

4.1 Methods and fit programs

The analysis has been made by means of the CERN-supported function minimization and error analysis program MINUIT. This program computes the best-fit parameter values and uncertainties, including correlations between the parameters. The function which should be minimized has to be provided by the user. In the present case this function varied depending on the number of components in the spectra (see Section 4.2). The communication with MINUIT was made via a Fortran program which read the data into an array and initialized the fit parameters. The user also has to decide in what region the fit should be made and if a bin factor should be used. The program provides the possibility to minimize the function to a given function according to the Pearson's χ^2 method, see Section 4.1.2, or by maximizing the log-likelihood function, see Section 4.1.1. The fit is made with MINUIT in an interactive mode which allows the setting of the parameter values as well as changing their statues on-line, between fixed and free. Being able to temporarily fix the value of a parameter can be a valuable tool to help MINUIT find a stable minimum for complicated functions containing several parameters.

For multi-parameter problems the parabolic errors are often only part of the truth. So in addition to parabolic error bars MINUIT provides so-called MINOS errors which also take parameter correlation and non-linearities into account. The one-sigma MINOS error for a given parameter is defined as the change in the parameter value which causes the minimized function to change with the value 1. What makes the MINOS errors more reliable than parabolic errors is that they consider the change with respect to all other free parameters. The meaning of one-standard deviation errors is that the true value with a probability of 68.3% lies between the error determinations. The correlation matrix tells the user how high the correlation between the different parameter values is. This is a very useful piece of information when evaluating the restrictions of information from the parameter estimate from the fit. The errors that have been given in Sections 4.3.2 – 4.3.5 are not parabolic errors but are based on the MINOS errors. This is not intended to be a detailed description of MINUIT; I herewith refer those readers who want to know more about MINOS errors and MINUIT in general to [MIN92].

In the following I have not presented any fits from binned spectra but only from fits of the original spectra with a channel width of 1 – 2 ms. Binning a spectrum can be useful if one wants to use a fit method which requires a certain number of counts per channel, for instance a χ^2 method. However, one should always keep in mind that one can never gain information by binning a spectrum but can only loose in resolution. The fact that the results are based on maximum likelihood minimizations does not mean that there were no χ^2 fits made. Both binned and unbinned χ^2 fits were made but did not provide any additional information for the parameter values to the maximum likelihood fits. However, they were very useful in providing an extra test of the hypothesis value to control that the data was really Poisson distributed via the χ^2 value. However, such a check was also provided with the maximum likelihood (see Section 4.1.1).

Finally, it should be pointed out that even though MINUIT is an excellent tool for fitting experimental data, it should not be forgotten that the chosen beamgates, measuring times and statistical properties of the data themselves represent the most important restrictions to the information that can be obtained from the data.

4.1.1   Maximum Likelihood

The most straightforward way of fitting experimental count numbers to a theoretical function is to maximize the probability, which is done with the maximum likelihood method.

$$L = \prod_i P(n_i|\theta_i) = \prod_i \theta_i^{n_i} e^{-\theta_i}/n! \ . \tag{4.3}$$

Let us first attempt to describe the process of fitting a constant spectrum and thus consider N_0 Poisson distributed random variables X_i, all with expectation value $E(X) = \mu$ and variance $Var(X) = \mu$. The advantage of using X_i rather than the count numbers n_i (the "function values" of X_i) is that one can then look not only at average properties, but also analyse the statistical fluctuations in the extracted fit values. As the likelihood function, L, is a product, the logarithm of the likelihood function, $\ln L$, is a sum which is often more convenient to handle. The log likelihood statistic is now

$$\ln L = \sum_{i=1}^{N_0} (X_i \ln \theta - \theta - \ln(X_i!)) \tag{4.4}$$

with derivative

$$\frac{\partial \ln L}{\partial \theta} = \sum_{i=1}^{N_0} (X_i/\theta - 1) \ . \tag{4.5}$$

The result of the fit is thus given by the random variable

$$\theta_L = \frac{1}{N_0} \sum_{i=1}^{N_0} X_i \ , \tag{4.6}$$

and is a simple average of Poisson distributions. Since the sum of Poisson distributions is a (new) Poisson distribution one can immediately write down the expectation value $E(\theta_L) = \mu$ and the variance $Var(\theta_L) = \mu/N_0$. A comparison between the expectation values for maximum likelihood, the Pearson and Neyman χ^2 methods can be seen in Figure 4.1.

An essential part of a fit is the goodness-of-fit test which tells us how good our model applies to the problem. For normal distributed variables a new function the χ^2 distance, η, is defined for this purpose.

$$\eta = \sum_i \frac{(X_i - \theta_i)^2}{(\sqrt{X_i})^2} \tag{4.7}$$

The new parameter, η, is χ^2 distributed [Råd84] and gives an estimate of the distance between an observable, X_i, and the estimate for the expected value, θ_i. This is the quantity which is minimized in the least square methods. When η is minimized its value can also be interpreted as a test of the goodness-of-fit. When the value for η, which is a sum over all channels, is divided by numbers of channels the values should be close to 1 for a satisfying goodness-of-fit test.

For the maximum likelihood method it is not as straightforward to get a goodness-of-fit estimate as with the χ^2 methods. However, with the powerful theorem on the likelihood ratio test for goodness-of-fit it is possible to construct another statistic. This enables one

to convert the likelihood function into a general χ^2 statistic. If μ_i are the true, unknown values of the parameters θ_i the likelihood ratio λ can be defined as

$$\lambda \;=\; L(X_i, \theta_i)/L(X_i, \mu_i) = \prod_i \frac{\theta_i^{X_i}}{X_i!} e^{-\theta_i} \Big/ \prod_i \frac{\mu_i^{X_i}}{X_i!} e^{-\mu_i} \,. \tag{4.8}$$

The likelihood test theorem says that "the likelihood χ^{2}" defined by

$$\chi_\lambda^2 \;=\; -2\ln\lambda = -2\ln L(X_i, \theta_i) + 2\ln L(X_i, \mu_i) \,, \tag{4.9}$$

asymptotically obeys a chi-square distribution. Note that the second term is independent of θ_i so that minimizing χ_λ^2 is entirely equivalent to minimizing the likelihood function L. The χ_λ^2 may then be used to estimate both the parameter value and goodness-of-fit test [Bak84].

We may replace the unknown μ_i with its bin-by-bin, model independent maximum likelihood estimate which is just X_i [Ead71] as referred to in [Bak84], which gives

$$\begin{aligned}
\chi_\lambda^2 \;&=\; 2\ln L(X_i, X_i) - 2\ln L(X_i, \theta_i) \\
&=\; 2\ln\left(\prod_i \frac{X_i^{X_i}}{X_i!} e^{-X_i}\right) - 2\ln\left(\prod_i \frac{\theta_i^{X_i}}{X_i!} e^{-\theta_i}\right) \\
&=\; 2\sum_i \left[\theta_i - X_i - X_i \ln\left(\frac{X_i}{\theta_i}\right)\right]
\end{aligned} \tag{4.10}$$

In practice it is actually more convenient to use this method than the normal logarithmic maximum likelihood as the $X_i!$ no longer has to be calculated.

4.1.2 Chi-square and low statistics

The classical and most widely used fit method in nuclear physics is the weighted least-square method, or the χ^2 method. It was popular due to the fact that it was relatively computer-friendly and it also has the advantage of giving a goodness-of-fit test. For normal distributed data the results from these fits are identical with the results when using the maximum likelihood method. However, the weighted least-square methods contain biases which become extremely important when working with low statistics. They will be investigated later in this section.

The different least-square methods are all based on the concept of minimizing the variance

$$\sum_i w_i(n_i - \theta_i)^2 \,. \tag{4.11}$$

Different choices for the weights w_i are used. Here two explicit examples are given:
the χ^2

$$\chi_P^2 = \sum_i (n_i - \theta_i)^2/\theta_i \,, \tag{4.12}$$

and the modified χ^2

$$\chi_N^2 = \sum_i (n_i - \theta_i)^2/n_i \,. \tag{4.13}$$

The names used for the former two statistics vary in physics literature; to avoiding confusion reference [Bak84] will be followed and they will be referred to as "Pearson's χ^2" and "Neyman's χ^2".

Pearson's χ^2 has the derivative

$$\frac{\partial \chi_P^2}{\partial \theta} = \sum_{i=1}^{N_0} \left(\frac{2(\theta - X_i)}{\theta} - \frac{(\theta - X_i)^2}{\theta^2} \right) \tag{4.14}$$

and is a minimum for

$$0 = \sum_{i=1}^{N_0} \left[2(\theta - X_i)\theta - (\theta - X_i)^2 \right] = \sum_{i=1}^{N_0} (\theta^2 - X_i^2) , \tag{4.15}$$

which gives

$$\theta_P = \sqrt{\frac{1}{N_0} \sum_{i=1}^{N_0} X_i^2} . \tag{4.16}$$

For Neyman's χ^2 one has the derivative

$$\frac{\partial \chi_N^2}{\partial \theta} = \sum_{i=1}^{N_0} \frac{2(\theta - X_i)}{X_i} = 2 \left[\theta \sum_{i=1}^{N_0} \frac{1}{X_i} - N_0 \right] , \tag{4.17}$$

which is minimum for

$$\theta_N = \left[\frac{1}{N_0} \sum_{i=1}^{N_0} \frac{1}{X_i} \right]^{-1} . \tag{4.18}$$

The expectation value and variance for θ_P and θ_N are given in Tables 4.1 and 4.2 for the lowest values of N_0. In both cases a bias is clearly seen in the expectation value, the deviations $|E(\theta) - \mu|$ increase with N_0 and are largest for θ_N. The variance decreases with increasing N_0, it is largest for θ_N and in both cases larger than the one for L. The best results are thus obtained when using L, and χ_P^2 is favoured to χ_N^2 (this ordering of the three methods is rather general [Ead71, Bak84]).

Asymptotic behaviour

For large N_0, the statistical fluctuations become unimportant (the variances go to zero) and the expectation values for the χ^2 statistics can be derived analytically. This is done by noting that the number of channels in the sum with the value k is $N_0 P(k|\mu)$. By reordering the summation one obtains for Pearson's χ^2

$$\chi_P^2 \rightarrow N_0 \sum_{k=0}^{\infty} P(k|\mu)(k - \theta)^2/\theta . \tag{4.19}$$

The derivative with respect to θ is easily calculated

$$
\begin{aligned}
\frac{1}{N_0} \frac{\partial \chi_P^2}{\partial \theta} &= \sum_{k=0}^{\infty} P(k|\mu)(1 - k^2/\theta^2) = 1 - \theta^{-2} \sum_{k=0}^{\infty} P(k|\mu)(k^2 - k + k) \\
&= 1 - \frac{\mu^2 + \mu}{\theta^2} .
\end{aligned}
\tag{4.20}
$$

The minimum in χ_P^2 is thus obtained for

$$\theta_P = \mu\sqrt{1 + 1/\mu} \simeq \mu + 1/2 \ . \qquad (4.21)$$

Fits with Pearson's χ^2 will systematically yield values which are too large.

The result for Neyman's χ^2 is slightly more complicated to derive since here one must safeguard against division by zero. From

$$\chi_N^2 \rightarrow N_0 \sum_{k=0}^{\infty} P(k|\mu)(k - \theta)^2 / \max(k, 1) \qquad (4.22)$$

one obtains the derivate

$$\frac{1}{N_0}\frac{\partial \chi_N^2}{\partial \theta} = 2\left[P(0|\mu)\theta + \sum_{k=1}^{\infty} P(k|\mu)(\theta/k - 1) \right] \ . \qquad (4.23)$$

The minimum is thus obtained for

$$\theta_N = \frac{1 - P(0|\mu)}{P(0|\mu) + \sum_{k=1}^{\infty} P(k|\mu)/k} \ , \qquad (4.24)$$

where for large μ one can approximate

$$\begin{aligned}
\sum_{k=1}^{\infty} \frac{P(k|\mu)}{k} &= \sum_{k=1}^{\infty} P(k|\mu)\left(\frac{1}{k+1} + \frac{1}{k} - \frac{1}{k+1} \right) \\
&\simeq \frac{1}{\mu} + \sum_{k=1}^{\infty} \frac{P(k|\mu)}{k(k+1)} \simeq \frac{1}{\mu} + \frac{1}{\mu^2}
\end{aligned} \qquad (4.25)$$

so that

$$\theta_N \simeq \frac{\mu^2}{\mu + 1} \simeq \mu - 1 \ . \qquad (4.26)$$

Fits with Neyman's χ^2 will yield values which are too small. Qualitatively, the biases in the two χ^2 statistics arise as follows. For Pearson's χ^2 the factor θ^{-1} clearly favours larger values of θ and gives an upward shift. For Neyman's χ^2 the k-values less than μ are weighted stronger than the ones larger than μ and this shifts the minimum downwards [Phi78, Awa79]. In [Awa79] a relation between the total areas of fit function and data was derived (for simple fit functions) that is similar to the asymptotic results just described. The present derivation is, however, more general and shows that the bias stems directly from the treatment of Poisson distributions with χ^2 statistics.

The asymptotic values just derived are also given in Tables 4.1 and 4.2. The results are also plotted as a function of μ in Figure 4.1 for all three statistics considered. The asymptotic deviations of -1 and +1/2 for χ_N and χ_P are seen to be good approximations down to μ about 10. Neyman's χ^2 is again the most deviant. In the figure, numerical results from Monte Carlo calculations are also given. Poisson distributed values were obtained by using random numbers generated with the CERNLIB routine RANMAR, and fits with the three different statistics were performed by MINUIT [MIN92]. Data sets ("spectra") of varying length N_0 were used. For each value of μ and N_0 the average over several data

Table 4.1: Pearson's χ^2. Expectation values and variances.

N_0	$\mu = 5$		$\mu = 10$		$\mu = 20$	
	$E(\theta)$	$Var(\theta)$	$E(\theta)$	$Var(\theta)$	$E(\theta)$	$Var(\theta)$
2	5.234	2.602	10.242	5.112	20.246	10.118
3	5.314	1.761	10.323	3.435	20.328	6.773
4	5.354	1.331	10.364	2.587	20.369	5.090
5	5.379	1.070	10.389	2.074	20.394	4.077
6	5.395	0.894	10.405	1.732	20.411	3.400
∞	5.477	–	10.488	–	20.494	–

Table 4.2: Neyman's χ^2. Expectation values and variances.

N_0	$\mu = 5$		$\mu = 10$		$\mu = 20$	
	$E(\theta)$	$Var(\theta)$	$E(\theta)$	$Var(\theta)$	$E(\theta)$	$Var(\theta)$
2	4.522	2.783	9.500	5.471	19.500	10.487
3	4.323	1.998	9.310	3.852	19.322	7.150
4	4.212	1.572	9.208	3.001	19.230	5.434
5	4.141	1.299	9.143	2.470	19.174	4.385
6	4.090	1.106	9.099	2.106	19.136	3.678
∞	3.780	–	8.844	–	18.940	–

sets were taken so that the final error on θ in all cases lie in the range 0.005 – 0.03. For small N_0 the minimization sometimes gave problems for very low values of μ; the lowest plotted points for $N_0 = 5$ therefore probably carry an additional systematic uncertainty. One should note that χ_N^2 converges much slower to the asymptotic values, both analytically and numerically, than χ_P^2.

To avoid these problems [Jam95], the expected number of events rather than the measured value is taken as a variance, in order to avoid bias toward lower values but to keep that variance constant during the fit. This is done to avoid the bias toward higher values as well as speeding up the fit. In practice this can be done in two ways; one is to take the average of the numbers of events in nearby bins as a variance. This is simple and independent of the fit hypothesis; it eliminates the first order bias effect and works well in practice, but is not strictly exact. The other is to take the starting value of θ for the fit hypothesis as a variance. This can then be refined by iteration, taking the fitted value of θ as a variance and then redoing the fit; in practice if the starting values were reasonable, this will not make a significant difference. The result of such an iteration should be as exact as one can get.
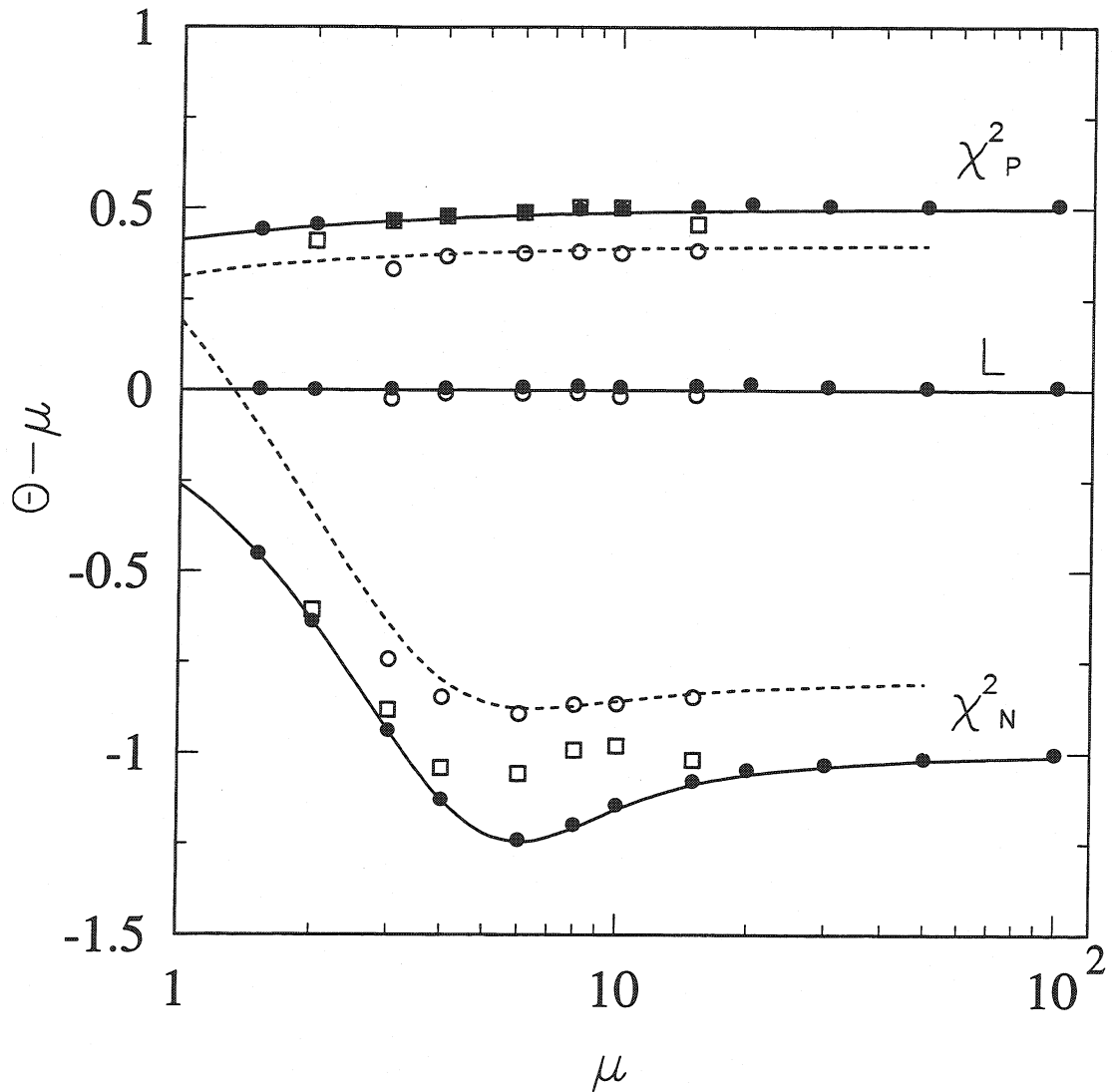
Figure 4.1: The difference between the fit estimate θ and the Poisson parameter μ is plotted versus μ for the two χ^2 statistics and for the maximum likelihood statistics; note the logarithmic scale. Solid lines are the asymptotic theoretical values for N_0 the large, broken lines are the ones for $N_0 = 5$. The points are results from Monte Carlo calculations with $N_0 = 5, 20, 10000$ (blank circles, blank squares, filled circles).

4.2 Principles of analysis

Up to now only the concept of fitting has been discussed without considering the theoretical model to which the data should be fitted. In this section, the functions describing the physics behind the count numbers measured in our experiments will be presented.

Decay of a radioactive nuclei is known to obey the following law

$$\frac{dN}{dt} = -\lambda N \tag{4.27}$$

where N is the number of nuclei and $\lambda = \ln 2/t_{1/2}$ the decay constant. As is well known, when using the initial condition $N(0) = C = N^0$ equation (4.27) can easily be solved by separation and integration and has the solution

$$N_1 = N_1^0 e^{-\lambda_1 t} \ . \tag{4.28}$$

This gives the final solution for the decay equation (4.27):

$$\frac{dN_1}{dt} = -\lambda_1 N_1^0 e^{-\lambda_1 t} \ . \tag{4.29}$$

When the daughter nuclei, N_2, are radioactive as well, the changes in number of nuclei follow the equation

$$\frac{dN_2}{dt} = \lambda_1 N_1 - \lambda_2 N_2 \ . \tag{4.30}$$

This is a linear first order differential equation with the general form

$$\frac{dN_2}{dt} + P(t)N_2 = Q(N_2) \ , \tag{4.31}$$

which can be solved according to a standard method (see reference [SMT84]),

$$N_2 e^{\int P(t)dt} = \int Q(t) e^{\int P(t)dt} dt + C \ , \tag{4.32}$$

where P(t) and Q(N_2) can be identified as P(t) = λ_2 and Q(N_2) = λ_1 N_1, and N_1 being given by equation (4.29):

$$
\begin{aligned}
N_2 e^{\int \lambda_2 dt} &= \int \lambda_1 N_1 e^{\int \lambda_2 dt} dt + C \\
N_2 e^{\lambda_2 t} &= \int \lambda_1 N_1^0 e^{-\lambda_1 t} e^{\lambda_2 t} dt + C \\
N_2 e^{\lambda_2 t} &= \int \lambda_1 N_1^0 e^{(\lambda_2 - \lambda_1)t} dt + C \\
N_2 e^{\lambda_2 t} &= \frac{\lambda_1}{\lambda_2 - \lambda_1} N_1^0 e^{(\lambda_2 - \lambda_1)t} + C \ .
\end{aligned}
\tag{4.33}
$$

In order to determine C, one has to use the initial condition

$$
\begin{aligned}
N_2(0) &= N_2^0 = \frac{\lambda_1}{\lambda_2 - \lambda_1} N_1^0 + C = 0 \\
C &= -\frac{\lambda_1}{\lambda_2 - \lambda_1} N_1^0 \ ,
\end{aligned}
\tag{4.34}
$$

which gives the following equation for N_2:

$$N_2 = \frac{\lambda_1}{\lambda_2 - \lambda_1} N_1^0 \left(e^{-\lambda_1 t} - e^{-\lambda_2 t} \right) \ . \tag{4.35}$$

If also the third generation of nuclei is radioactive, this granddaughter activity can be written analogous to the daughter activity

$$\frac{dN_3}{dt} = \lambda_2 N_2 - \lambda_3 N_3 \tag{4.36}$$

and can then also be solved in an analogous way; see equation (4.32) – (4.35). This gives the following solution

$$N_3 = \frac{\lambda_1 \lambda_2}{\lambda_2 - \lambda_1} N_1^0 \left[\frac{1}{(\lambda_3 - \lambda_1)}(e^{-\lambda_1 t} - e^{-\lambda_3 t}) - \frac{1}{(\lambda_3 - \lambda_2)}(e^{-\lambda_2 t} - e^{-\lambda_3 t}) \right] . \qquad (4.37)$$

When halflives are determined with beta-delayed neutron spectra, an additional term is introduced, as only a fraction of all beta decays are followed by neutron emission. This term is the beta-delayed neutron emission rate, the P_n value, which normally takes values between 0 and 100%. However, values slightly above 100% can also be reached as the P_n value is defined as the number of neutrons emitted per beta decay [1]. It is also possible that 2 or 3 neutrons are emitted from the same nucleus although these modus have a smaller probability than the one neutron emission.

For masses 120 – 126, indium isotopes do not yet emit neutrons. This makes the fit functions very simple for these masses. They only contain one exponential decay and a constant background, C,

$$\frac{dN^{tot}}{dt} = \lambda(Ag) \cdot P_n(Ag) \cdot N^0(Ag)e^{-\lambda(Ag)t} + C . \qquad (4.38)$$

In practice the product $P_n(Ag) \cdot N^0(Ag)$ was determined, as the $P_n(Ag)$ values were not known and could not be determined; see Section 3.3.2.

At A = 127, besides silver also the beta decay granddaughter indium starts emitting beta-delayed neutrons, whereas the Cd-daughters are not yet delayed-neutron precursors. At this mass compared to silver the primary ionized indium was already so abundant that the secondary produced indium, the granddaughter from ^{127}Ag, could be neglected in the fit. The fit function was then simplified to the following expression:

$$\frac{dN^{tot}}{dt} = \lambda_1 \cdot P_n(Ag) \cdot N_3^0 e^{-\lambda_1 t} + \lambda_3 \cdot P_n(In) \cdot N_3^0 e^{-\lambda_1 t} + C . \qquad (4.39)$$

Also here the terms $P_n \cdot N^0$ were in practice fitted with N^0. For ^{128}Ag the fit function becomes somewhat more complicated as also the granddaughter decay i.e. ^{128}In was taken into account in accordance to equations (4.36) and (4.37):

$$\frac{dN^{tot}}{dt} = \lambda_1 \cdot P_n^1 \cdot N_1^0 e^{-\lambda_1 t} + \lambda_3 \cdot P_n^3 \cdot N_3^0 e^{-\lambda_3 t} + \lambda_3 \cdot P_n^3 \cdot [1 - P_n^1] \frac{\lambda_1 \lambda_2}{\lambda_2 - \lambda_1} N_1^0 \qquad (4.40)$$

$$\times \left[\frac{1}{(\lambda_3 - \lambda_1)}(e^{-\lambda_1 t} - e^{-\lambda_3 t}) - \frac{1}{(\lambda_3 - \lambda_2)}(e^{-\lambda_2 t} - e^{-\lambda_3 t}) \right] + C .$$

An additional complication in the fits are possible isomers in both Ag and In isotopes. Beta-decaying isomers originate from excited states in nuclei from which γ-decay is strongly hindered due to large differences in spin. The beta decay from the isomers

---

[1] The P_n value can also be explicitly defined as ratios of one, two and three neutron emission per beta decay. These P_n values are then denoted by P_{1n}, P_{2n} and P_{3n}.

to considered here can, like beta decay from ground states, emit beta-delayed neutrons.

To find out if one can expect any isomers in the heavy silver isotopes it is useful to review the nuclear structure of experimentally known silver isotopes closer to stability. Considering also other nuclei in the mass region can further contribute to the understanding of the nuclear structure of the silver isotopes [Wal95]. In principle there are two cases involved in particle structure, namely the odd-mass isotopes and the odd-odd isotopes.

The spin and parity of odd-mass isotopes are determined by the unpaired particle or, in the case of an almost full shell, an unpaired hole. Indium with 49 protons is just one proton away from the magic tin which has a full $g_{9/2}$ proton shell. Consequently, the ground state of the spherical indium isotopes is known to have spin and parity $I^\pi = 9/2^+$. However, there is also an isomeric proton p1/2$^-$ level which is situated some 300 keV above the ground state in ^{125,127,129}In. For ^{127,129}In this isomeric level is known to emit beta-delayed neutrons.
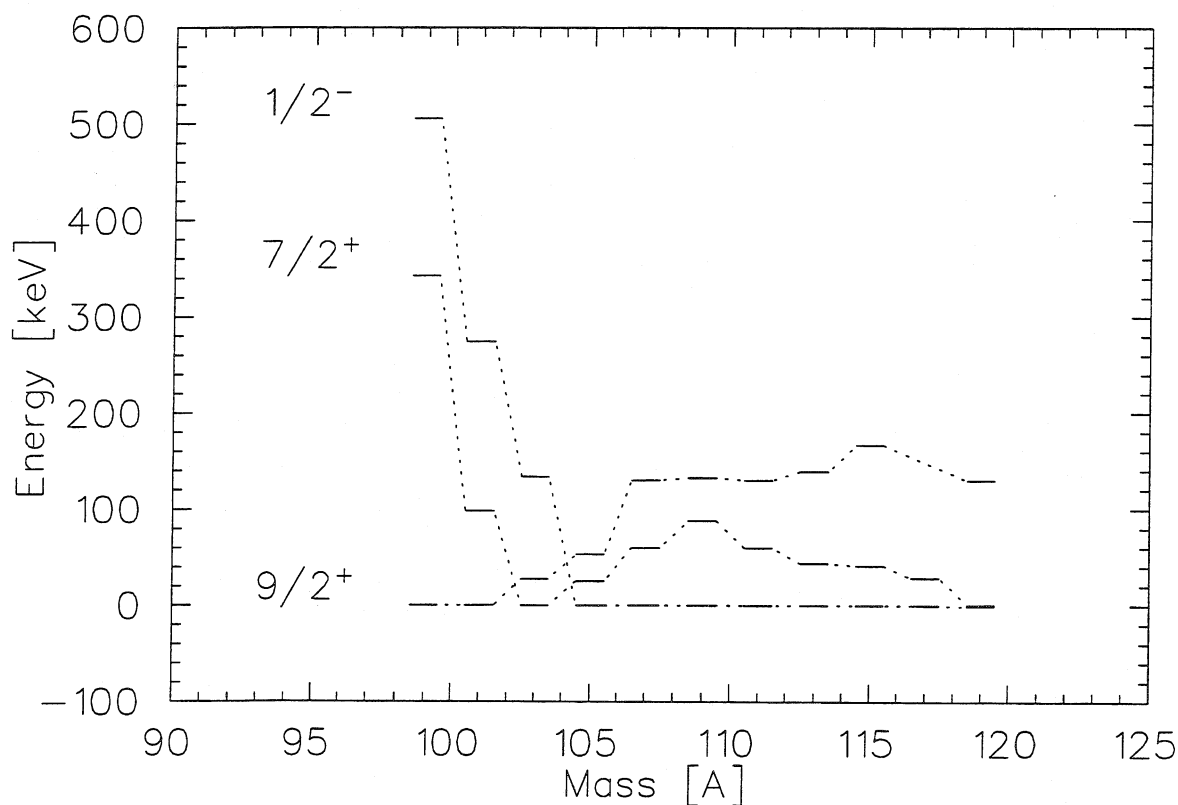

Figure 4.2: Experimentally-observed 1/2$^-$, 9/2$^+$ and 7/2$^+$ proton levels in the odd-mass silver isotopes $^{99-119}$Ag. The levels have been taken from recent Nuclear Data Sheets.

In silver with three proton holes the situation is somewhat more complicated. In addition to the 9/2$^+$ and 1/2$^-$ states the three $g_{9/2}$ proton holes can couple to a 7/2$^+$ cluster state; see Figure 4.2. In the proton-rich ^{99,101}Ag isotopes this 7/2$^+$ level is known to lie above the 9/2$^+$ state but below the 1/2$^-$ level. Therefore, the 1/2$^-$ level can decay via an E3 internal transition to the 7/2$^+$ level and does not form an isomer. The result is only one beta-decaying level, i.e. from the 9/2$^+$ ground state. Going above the closed N = 50 shell,

the $1/2^-$ level becomes the ground state in $^{105-117}$Ag but the $7/2^+$ level also lies below the $9/2^+$ level here. This again makes an E3 transition possible which partly decays via internal transition and partly via beta decay in these isotopes.

For the neutron-magic ^{131}In the ground state is $9/2^+$ with the $1/2^-$ state some 300 keV above [Fog84]. Removing two protons will certainly change the spacing between the two levels but it is unlikely that the effect is so pronounced so that the $9/2^+$ state would no longer lie below the $1/2^-$ state in the N = 82 isotone ^{129}Ag. With this argument one can assume that the ground state of ^{129}Ag is $9/2^+$. In that case the position of the $7/2^+$ level determines whether there will be an isomer or not. If it lies below the $1/2^-$ level there will be an E3 internal transition possible and no beta-decaying isomer. However, if the $7/2^+$ level lies above the $1/2^-$ state, the internal transition would be M4. Such a low-energy γ-transition is so hindered that the $1/2^-$ level will deexcite via beta decay.

For odd-odd silver isotopes it is difficult to make detailed predictions as there are several possibilities. The three proton holes can couple with the neutron holes to a large number of states. The two most probable are: $\pi g_{9/2}$, $\nu h_{11/2}$, forming a negative-parity high-spin isomer and $\pi g_{9/2}$, $\nu d_{3/2}$ with antiparallel coupling, forming a $I^\pi = 3^+$ state. In addition, $\pi p_{1/2}$ holes couple with $\nu h_{11/2}$ and $\nu d_{3/2}$ neutrons. However, in the odd-odd silver isotopes $^{116-120}$Ag two beta-decaying states are known [Fog71]. In the heavy odd-odd indium isotopes there are also at least two beta-decaying states observed and in ^{130}In even three [Fog81]. This makes it probable that there are also at least two beta-decaying states in the heavy odd-odd silver isotopes, $^{122-128}$Ag.

4.3 Results

Before going into details of the analysis for the different isotopes a few general remarks
have to be made on the spectra themselves.

In Table 4.3 the results from the halflife analyses for $^{120-128}$Ag have been listed, together
with earlier halflife measurements made with β-delayed neutrons, β- or γ-detection.

Table 4.3: Halflives for silver isotopes $^{120-128}$Ag from this and earlier publications.

Isotope	Halflives [ms]			Method	Reference
^{120}Ag	1350	$\pm$	200	n	This thesis
	1250	$\pm$	30	β	[Ree83]
	1170	$\pm$	50	γ	[Fog71]
^{121}Ag	1010	$\pm$	100	n	This thesis
	910	$\pm$	60	n	[Ree83]
	780	$\pm$	10	β	[Ree83]
	720	$\pm$	100	β	[Fog82]
	800	$\pm$	100	γ	[Gra74]
^{122}Ag	520	$\pm$	20	n	This thesis
	570	$\pm$	30	n	[Ree83]
	480	$\pm$	80	γ	[Shi78]
	1500	$\pm$	500	γ	[Fog71]
^{123}Ag	293	$\pm$	6	n	This thesis
	300	$\pm$	10	n	[Ree83]
	390	$\pm$	30	n	[Lun76]
	300	$\pm$	20	γ	[Mac86]
^{124}Ag	172	$\pm$	5	n	This thesis
	540	$\pm$	80	n	[Ree83]
	170	$\pm$	30	γ	[Hil84]
^{125}Ag	155	$\pm$	7	n	This thesis
^{126}Ag	98	$\pm$	3	n	This thesis
^{127}Ag	79	$\pm$	3	n	This thesis
^{128}Ag	58	$\pm$	5	n	This thesis

In the analysis of the heavier silver isotopes, halflives and P_n values for Cd and In iso-
topes were taken into account. In Section 4.3.6 these values are also used for estimates of
production rates. In Table 4.4 selected data from experiments with respective references
are summarized.

Table 4.4: Halflives and P_n values for neutron-rich Cd and In isotopes.

Isotope (I^π)	Halflives [s]			P_n	Reference
^{127}Cd	0.43	$\pm$	0.03	-	[Gök86]
^{127}Cd	0.30	$\pm$	0.03	-	[Mac86]
^{127}In ($1/2^-$)	3.8			0.68 ± 0.06	[Lun80]
^{127}In ($1/2^-$)	3.8	$\pm$	0.2	-	[Gök86]
^{127}In ($9/2^+$)	1.12	$\pm$	0.02	< 0.04	[Lun80]
^{127}In ($9/2^+$)	1.22	$\pm$	0.05	-	[Gök86]
^{128}Cd	0.34	$\pm$	0.03	-	[Gök86]
^{128}In (3^+)	0.84	$\pm$	0.06	-	[Gök86]
^{128}In (8^-)	0.72	$\pm$	0.1	-	[Gök86]
^{128}In (mix)	0.80			0.059 ± 0.008	[Lun80]
^{129}Cd	0.27	$\pm$	0.04	-	[Gök86]
^{129}Cd	0.26	$\pm$	0.02	-	[Mac86]
^{129}In ($1/2^-$)	1.30	$\pm$	0.1	-	[Gök86]
^{129}In ($1/2^-$)	1.26	$\pm$	0.02	2.5 ± 0.5	[Lun80]
^{129}In ($9/2^+$)	0.68	$\pm$	0.05	-	[Gök86]
^{129}In ($9/2^+$)	0.59	$\pm$	0.02	0.25 ± 0.5	[Lun80]

In the sections for the isotopes with isobaric indium some production ratios between nuclei with different halflives are given. These estimates are made for the collection time which was found to be appropriate for that specific measurement. If a longer beamgate was used, the number of long-lived nuclei would increase compared to the short-lived nuclei. More nuclei of both types would have time to release from the target but at the same time more short-lived nuclei would have decayed. The absolute production ratios are also dependent on the production method. It can thus be seen that the ratios observed at ISOLDE with proton induced fission differ from the ratios obtained with other methods. Despite these limitations the figures might have a value for further experiments in this region.

Analyzing the singles spectra, especially the ones taken during the second beamtime in July 1995, contained an unexpected difficulty. The longer 4K spectra contained several spikes. They appeared in all neutron spectra from all three detector rings and approximately in the same channels. Most likely these spikes and extra counts were produced in the histogramming memory modules.

These spikes have been treated in the following way. A simple weighted fit according to Neymans χ^2 method has been laid through the data points, containing a constant back-

ground and one, respectively two exponential components. It has been visually checked that the result was acceptable. Then each data point has been compared with the χ^2 fit in that channel and data points containing count rates with probabilities smaller than 10^{-4} have been defined as spikes and have not been considered in the fit. This was up to 30 channels out of 4096, mostly single channels but sometimes up to 3 channels next to each other. One does not necessarily remove all influence from the spikes with this method. A certain distortion of the spectrum can remain. This is in particular a problem for isotopes with somewhat longer halflives in combination with low statistics. The remaining spikes, which were placed at the end of the spectrum in particular, could lead to the result that the fitted halflife became longer than the true halflife. This seems to be the case for ^{120}Ag, see Section 4.3.2. The remaining spikes were also visible in spectra with short halflives where only the cosmic background should be left at the end of the spectrum. However, extra counts in this region are less serious, as the constant background could always be controlled and well estimated from the number of cycles.

4.3.1 Background

Low neutron background level and a correct estimate of this level was essential for the analysis. Owing to the pulsed operation of the accelerator, the background during the measurements could be reduced compared to earlier experiments at the former SC-ISOLDE. The background could be clearly divided into two components, the constant and rather low background induced through cosmic radiation and a second component of prompt neutrons originating from the proton pulse hitting the target; see Figure 4.3. The "halflife" of this prompt, beam correlated component was determined to 10.9 ± 0.2 ms at beamline LA1. This fortunately meant that this component had no influence on the decay part of the spectra which was used for the halflife fits.
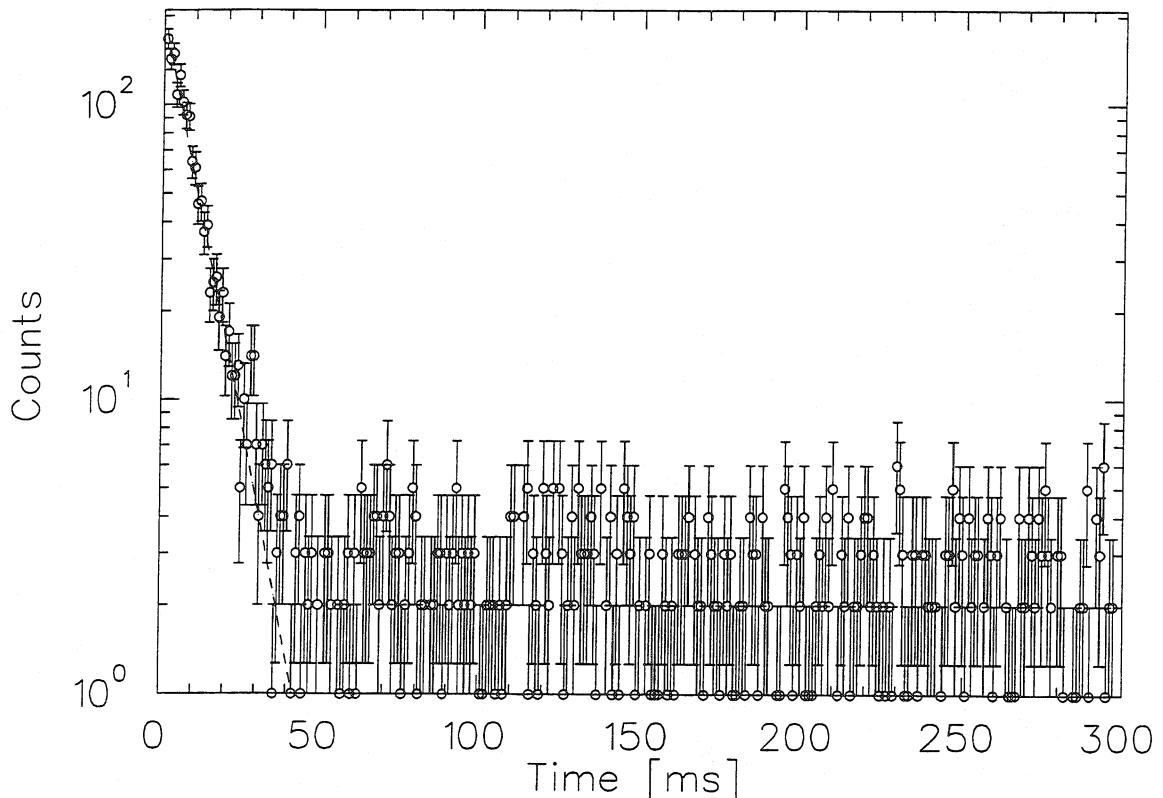

Figure 4.3: Fast neutrons correlated with the proton pulse with $T_{1/2} = 10.9 \pm 0.2$ ms and constant background from cosmic radiation. The spectrum contains 3340 measuring cycles with all three detector rings.

The only background component, with exception of the isobaric contamination from indium starting at mass 127, was thus the cosmically induced background which could be determined with very good accuracy. For the whole long-counter with all three detector rings, including 50 ^{3}He-tubes, 0.735 ± 0.01 neutrons per 1.024 s were registered. When only the two inner rings containing a total of 42 tubes were used, as in the spectra of ^{128}Ag, 0.605 ± 0.01 neutrons per 1.024 s, were registered.

The number of cycles were registered during the measurements which gave a good estimate of the cosmically induced background component. In many of the spectra it was

also possible to leave the background as a free parameter during the fit. However, for spectra where the measuring time was short compared to the halflives of the isotopes or for spectra with many components or many spikes, it was essential to have a good estimate of the background level. When the background had to be kept fixed during the fit, several fits were made with different assumptions on the background level to find out how sensitive the halflife estimates were to this parameter.

4.3.2 $^{120-126}$Ag

The spectrum at A = 120 was taken with a collection time of 600 ms; the total spectrum was 4.1 s long and had about 10 counts per ms in the peak. The measuring time was relatively short compared to the halflife and the count rate was low which is why remaining spikes distorted the spectrum; see Section 4.3. Due to these effects the determination halflife has rather large uncertainties. However, it can be clearly seen from the halflife determined that the neutrons are emitted from the ground state as was proposed in [Ree83].
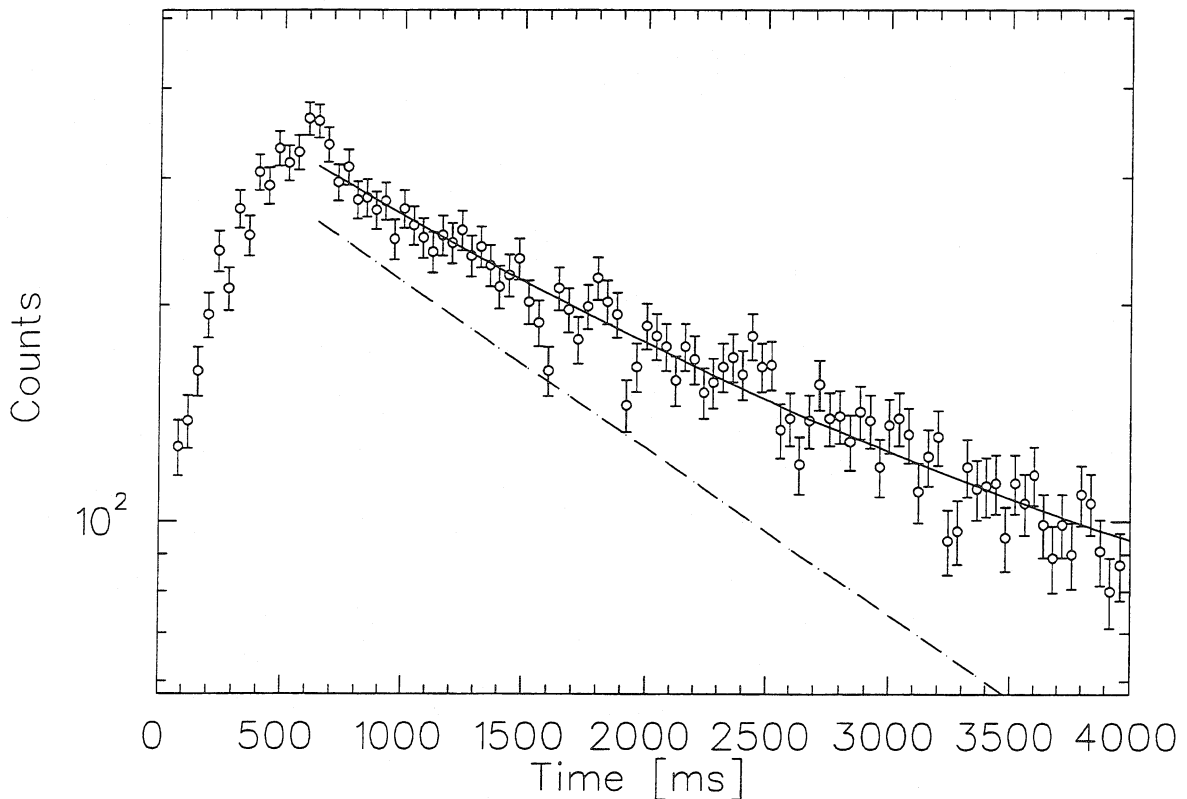

Figure 4.4: Beta-delayed neutrons from ^{120}Ag with $T_{1/2}(^{120}$Ag$) = 1.3$ s. The solid line represents fit and background. The broken line is the pure silver component. The original data were binned with a factor of 40. The logarithmic y-axis goes from 60 to 500.

The fits where the background was fixed to the expected value based on the number of measuring cycles gave a halflife of 1.4 s. However, when the background was left as a free parameter it was overestimated by some 25% compared to the expected value and the halflife became correspondingly shorter. The assumption in reference [Ree83] that

the spectrum consists of one silver component can be confirmed and this component has been fitted to $T_{1/2}(^{120}\text{Ag}) = 1.3 \pm 0.2$ s. In Figure 4.4 the binned neutron spectrum, taken with three detector rings and without spikes with the $T_{1/2}(^{120}\text{Ag}) = 1.3$ s fit, has been plotted with one data point per 40 ms. The broken line is the silver component after background subtraction.

The measurements for A = 121 and A = 122 were taken during a rapid mass scan because these halflives were already known. The purpose of the mass scan was to get a measure of the progression of the production and neutron emission rates with increasing mass. The measuring time in the spectra of the mass scan was 1 s in total, of which 300 ms were collection time, with 1 ms per channel. The short counting time is the reason for the relatively large error bars. This also made it impossible to fit the background as a free parameter. For ^{121}Ag the halflife $T_{1/2}(^{121}\text{Ag}) = 1.01 \pm 0.1$ s was determined from a spectrum with some 30 counts per ms in the peak and for ^{122}Ag $T_{1/2}(^{122}\text{Ag}) = 520 \pm 20$ ms was determined from a spectrum with some 50 counts per ms in the peak. These halflives are in agreement with earlier measurements with β-delayed neutrons from reference [Ree83], i.e. 910 ± 60 ms for ^{121}Ag and 570 ± 30 ms for ^{122}Ag. The possibility of isomers in odd-odd silver isotopes has been discussed at the end of Section 4.2. In reference [Zam95] two beta-decaying states with halflives of 1.5 s and 0.48 s are mentioned, unfortunately without a reference. The only further information about a possible long-lived isomer that I have been able to find is in [Fog71]. There, an 1.5 ± 0.5 s halflife based on some 10 γ-events is reported. The halflife from the two measurements with beta-delayed neutrons are somewhat longer than the halflife of ^{122}Ag adopted in recent Nuclear Data Sheets, 480 ms [Shi78]. This could be an additional indication that the neutrons observed originate from two beta-decaying states.

For mass A = 123, 1 s and 2 s spectra were taken with 1 or 2 ms respectively per channel and 300 ms collection time. The 2 s spectrum with the best statistics had some 90 counts per ms in the peak. In the fits of this spectrum, the background could be fitted as a free parameter and was found to be in good agreement with the expected value. The halflife determined for this silver isotope was $T_{1/2}(^{123}\text{Ag}) = 293 \pm 6$ ms which fits well with the two latest measurements made on this isotope, neutron measurements from [Ree83] and γ-measurements from [Mac86]; see Table 4.3.

For mass A = 124, the spectra were taken with a measuring time of 2 s and 2 ms per channel and the fit of the decay was started after 300 ms. The best fit was obtained from a spectrum with 64 counts per ms in the peak. This spectrum with the fitted halflife is shown in Figure 4.5 binned with a factor of 10. The fitted background was in good agreement with the expected one and the ^{124}Ag spectra could be fitted with one silver component with $T_{1/2}(^{124}\text{Ag}) = 172 \pm 5$ ms. This is the heaviest silver isotope for which earlier halflife measurements exist. The neutron measurement of [Ree83] gives a halflife of 540 ± 80 ms. This value cannot be reproduced which is somewhat surprising even when considering that the earlier halflife estimate was made with rather bad statistics. There are also halflife measurements made with γ-detection [Mac86] in existence which give a value of 170 ± 30 ms, in agreement with this thesis, see Table 4.3. However, also at this mass it is possible that the neutrons originate from two different Ag isomers but probably with very similar halflives.
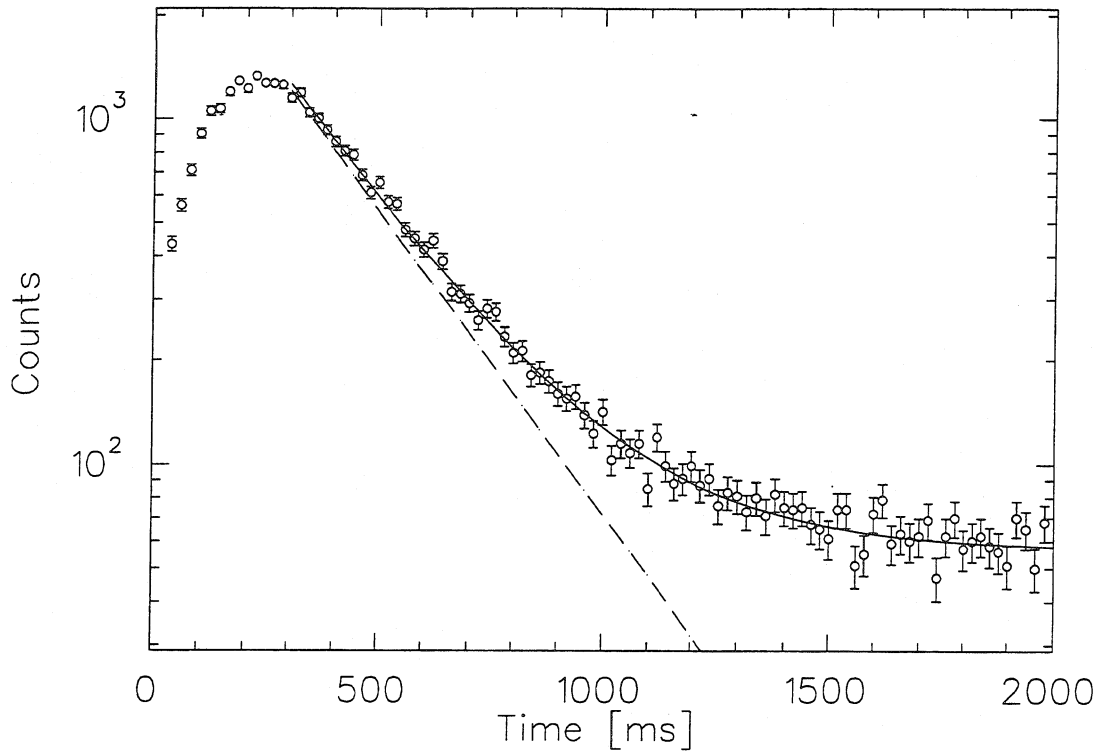
Figure 4.5: Beta-delayed neutrons from ^{124}Ag with a $T_{1/2}(^{124}$Ag$) = 172$ ms fit. The solid line represents fit and background. The broken line is the pure silver component.
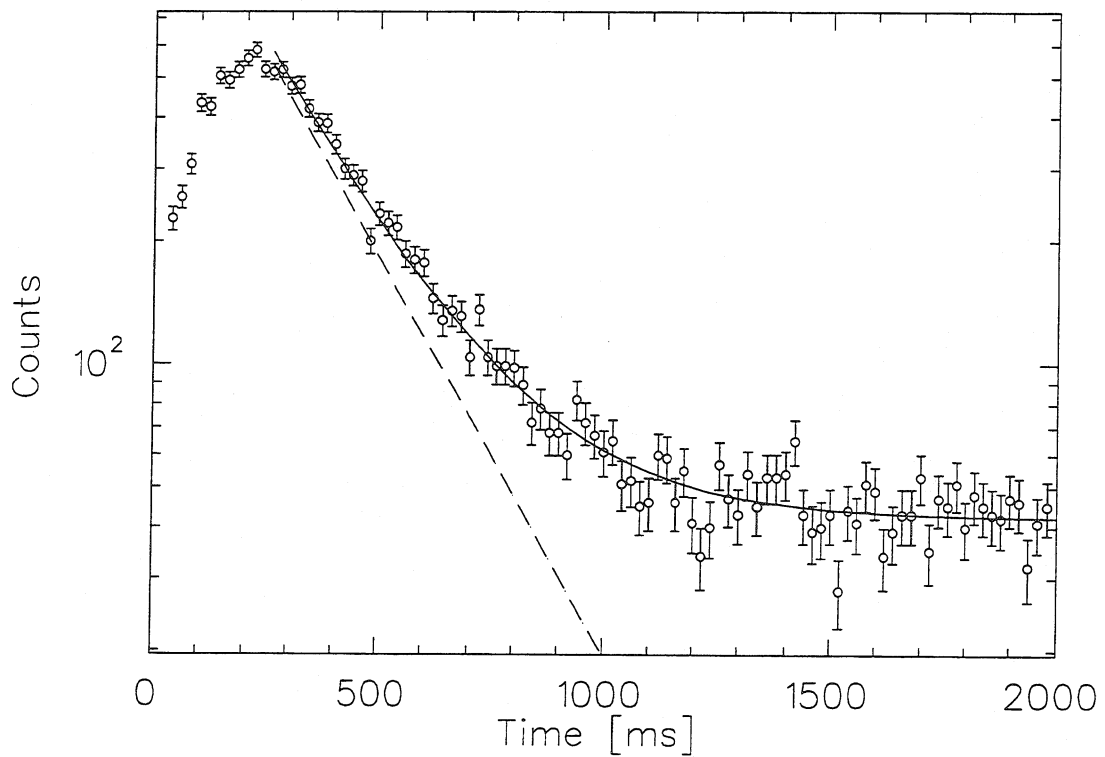

Figure 4.6: Beta-delayed neutrons from ^{125}Ag with $T_{1/2}(^{125}$Ag$) = 155$ ms fit. The broken line is the pure silver component and the solid line also contains the background.

The isotope ^{125}Ag was the lightest of the silver isotopes which was observed for the first time in the first part of the IS333 experiment. The statistics were still fairly good and the background fits were in good agreement with the expected value for the background. The analysis was made with 2 s long spectra taken with 250 ms collection time. The total added spectrum had 50 counts per channel, 25 per ms, in the peak. From this spectrum a halflife of $T_{1/2}(^{125}Ag) = 155 \pm 7$ ms was determined for ^{125}Ag; see Figure 4.6.
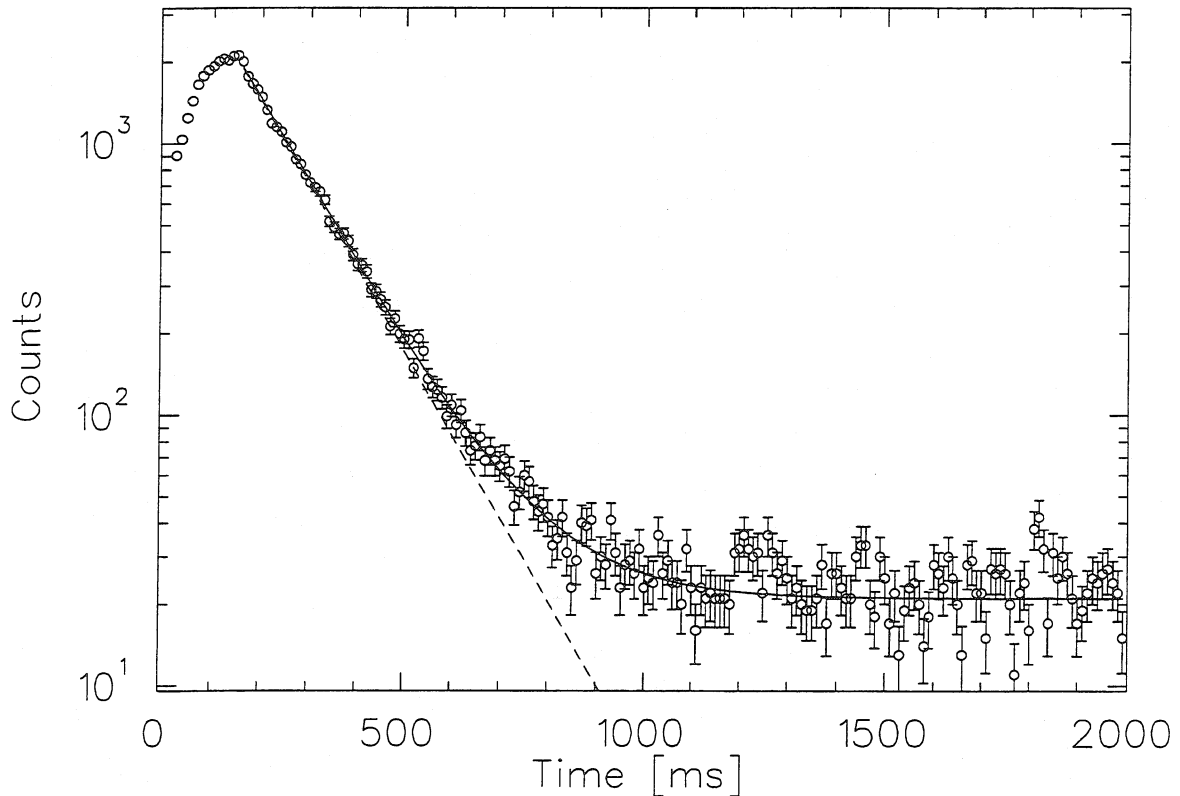

Figure 4.7: Beta-delayed neutrons from ^{126}Ag with a $T_{1/2}(^{126}Ag) = 98$ ms fit (solid line). The broken line is the silver component without the background.

For ^{126}Ag, the first part of the experiment gave a rather poor statistics. Due to this the halflife was originally determined to be longer than the halflife given here, which was determined from data from the second beamtime. These spectra could be fitted with only one exponential decay component of $T_{1/2}(^{126}Ag) = 98 \pm 3$ ms and a constant background component, such as for the lighter isotopes. In Figure 4.7, data from some four hours of measurement from the second experiment with a $T_{1/2}(^{126}Ag) = 98$ ms fit are shown. The original data have been binned with a factor of 10 which gives one data point per 10 ms in the spectrum. The original data had some 210 counts per 1 ms channel in the peak. Also for this even-A isotope, the emitted neutrons might originate from two isomers as for ^{122}Ag and ^{124}Ag.

4.3.3 ^{127}Ag

The measurements for ^{127}Ag were the first test for the selectivity of the laser ion source, as ^{127}In is the lightest In isotope which emits neutrons. For the lighter isotopes the increased ionization efficiency for silver was primarily used, as indium did not disturb the neutron measurements at those masses. The first IS333 beamtime made it possible to identify a silver component but the halflife was considerably overestimated [Fed95] due to poor statistics of silver and an overpowering isobaric background of indium. According to [Lun80], the neutrons from indium originate from two different isomers.

^{127}In($1/2^-$)	3.8 s	$P_n = 0.68 \pm 0.06$
^{127}In($9/2^+$)	1.12 ± 0.02 s	$P_n \leq 0.04$

If the different spin states were produced with the same ratio, the 1.12 s component should be observed some 20 times weaker than the 3.8 s component. Fitting the two components with fixed halflives and background, gave ratios between 95 and 225. This is in agreement with the observation that the production of low spin isomers is normally favoured at ISOLDE. For the fit, an average indium halflife was determined from the "laser-on" spectra, $\overline{T}_{1/2}(^{127}\mathrm{In}) = 3595 \pm 30$ ms. This value agreed well with the fits from spectra taken without the lasers but with an identical length of 4096 ms and a collection time of 150 ms. However, the determined silver halflife was not very sensitive to variations of $\overline{T}_{1/2}(^{127}\mathrm{In})$. Despite problems with spikes, the second beamtime with the increased laser ionization efficiency and silver production rates gave good statistics for a halflife determination for ^{127}Ag of $T_{1/2}(^{127}\mathrm{Ag}) = 79 \pm 3$ ms.
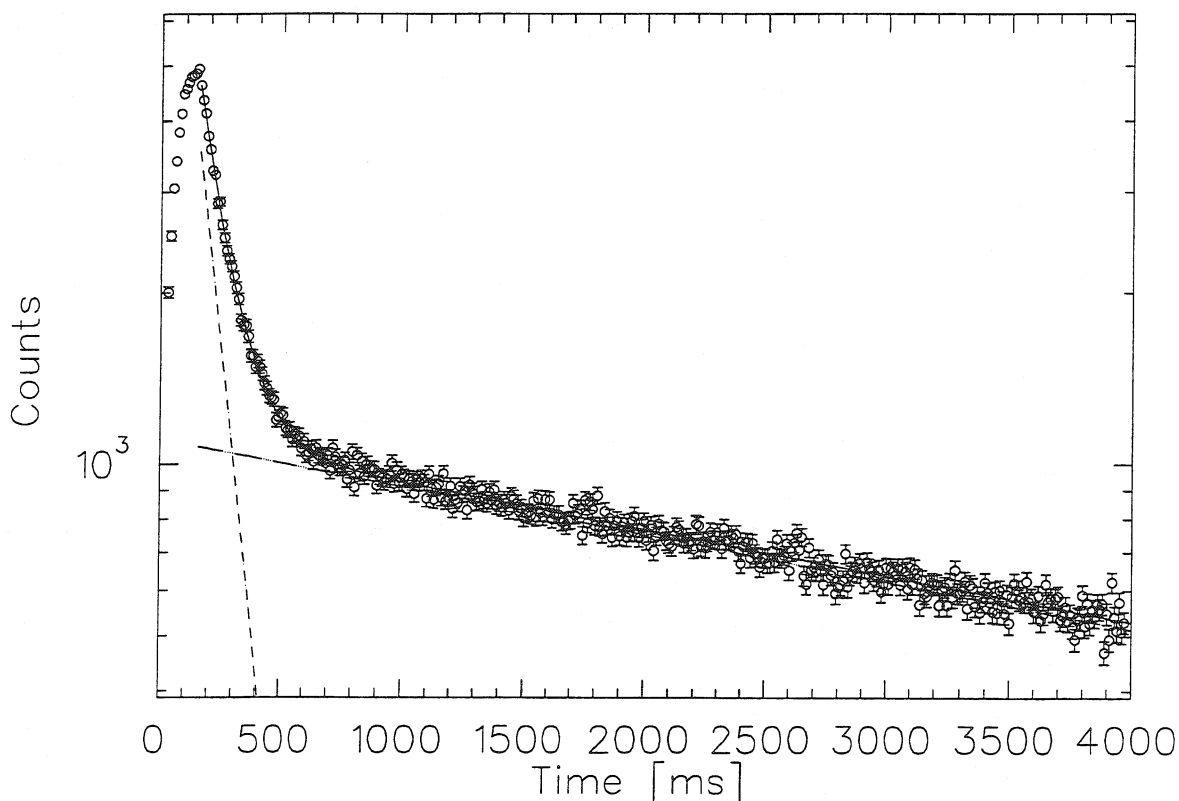

Figure 4.8: Beta-delayed neutrons from ^{127}Ag and ^{127}In (solid line). The short broken line represent the Ag component and the long broken line the In component.

4.3.4 ^{128}Ag

According to reference [Gök86], there are two In isomers with halflives very close to each other, $T_{1/2}(^{128}In(3^+)) = 840 \pm 60$ ms and $T_{1/2}(^{128}In(8^-)) = 720 \pm 100$ ms. Not knowing the exact production rate and the P_n values, it is impossible to separate the two components without gamma measurements. However, as for ^{127}In an average halflife of the two tabulated values has been determined $\overline{T}_{1/2}(^{128}In)$. It should be made clear that $\overline{T}_{1/2}(^{128}In)$ can vary with collection time and production facility, so it was taken as a specific fit parameter for the conditions of these measurements.

At this mass, it makes sense to use just the two inner rings of the neutron detector as the outer one has a more unfavorable In-to-Ag ratio. The background had to be estimated accordingly; see Section 4.3.1. For this mass, a new fit function taking the granddaughter activity into account was implemented; see Section 4.2. The reason was that during the run the spectra without the lasers were subtracted from the spectra taken with the lasers. This differential spectrum did not only show a beautiful Ag-component but also something that looked like an ingrowing In-component. However, after closer analysis and corrections for spikes I am no longer convinced that this effect is as large as it was believed. The visual effect was rather due to unfortunate positioning of spikes and extra counts, in conjunction with the fact that the spectra were not multiplied with the correct factor before the subtraction. In addition, the production rates were somewhat different between the two spectra due to different proton intensity. This is a problem as the
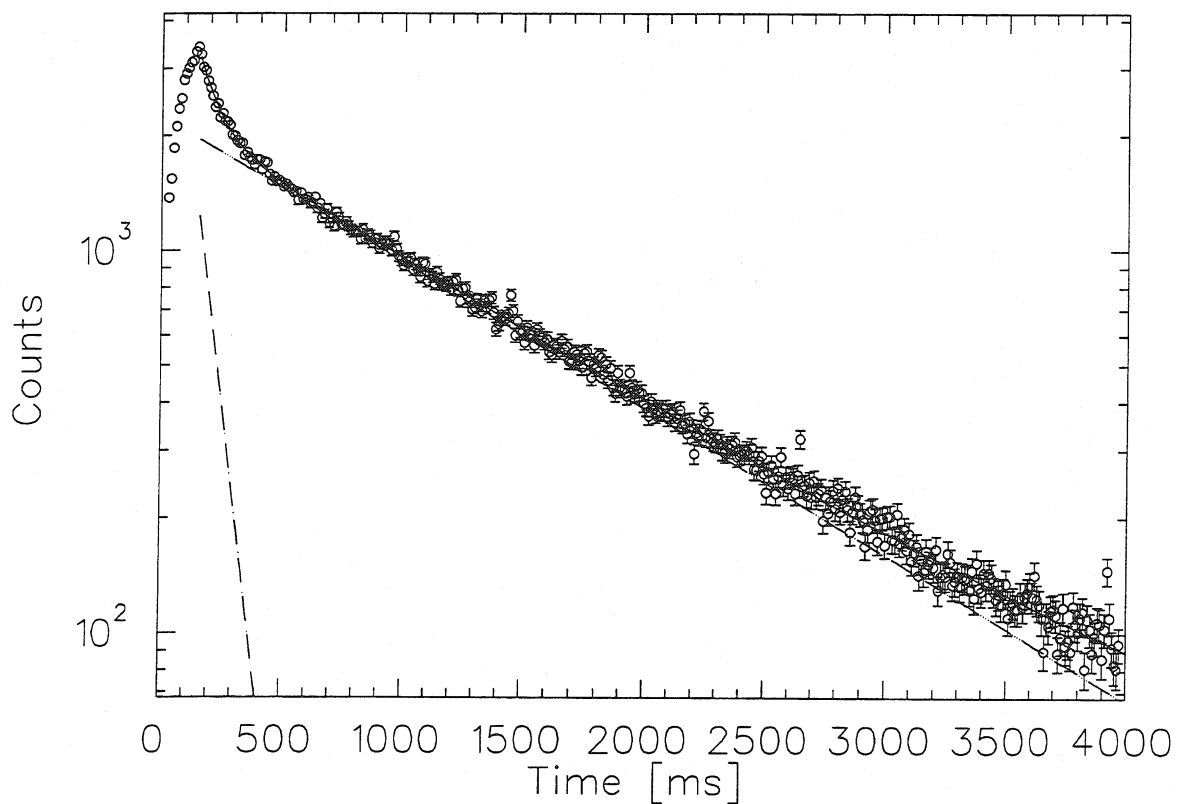

Figure 4.9: Beta-delayed neutrons from ^{128}Ag and ^{128}In. The short broken line is the silver component and the long broken line is the average indium component.

background is strictly time independent. Attempts to subtract the backgrounds and then subtract the spectra has not led to any positive results.

The P_n dependent pre-factor $[1\text{-}P_n^1] \cdot P_n^3$ to the granddaughter activity was allowed to vary between 0 and 1. However, it could not be left as a free parameter during the fit as it would take unphysical values. The same holds for $T_{1/2}(^{128}\text{Cd})$. Fortunately, the fits were not very sensitive to these parameter, so I have used $T_{1/2}(^{128}\text{Cd}) = 260$ ms [Mac86] as a standard value. The $\overline{T}_{1/2}(^{128}\text{In})$ was rather stable with 792 ± 7 ms. This value is in good agreement with the values from spectra without the lasers $\overline{T}_{1/2}(^{128}\text{In}) = 794 \pm 8$ ms.

Several different fits have been made on this spectrum, varying from full granddaughter activity, $P_n(^{128}\text{Ag}) = 0$ and $P_n(^{128}\text{In}) = 1$, to zero granddaughter activity. The background has been varied around the calculated value and fitted as a free parameter. All fits give the same results: $T_{1/2}(^{128}\text{Ag}) = 58 \pm 3$ ms. The fitted background is also very close to the expected background and the fit is very stable. However, also in this spectrum there were problems with spikes. Taking these factors into account, the following halflife and uncertainty were determined $T_{1/2}(^{128}\text{Ag}) = 58 \pm 5$ ms. In Figure 4.9, a spectrum where the spikes have been taken away is shown with the fits for the Ag and In components.

4.3.5 Measurements at mass 129

As has been discussed earlier in this chapter, it is difficult to predict what the level structure in ^{129}Ag will look like and thus what halflife can be expected. In order to cover several possibilities, the measurements at mass 129 were made with two collection times; a 1 s spectrum with 80 ms collection time and a 4 s spectrum with 200 ms collection. However, the spectra could be well fitted with only two exponential components with halflives in good agreement with γ measurements [Gök86] for the two indium isomers; see Table 4.4. The background had to be kept fixed during the fits due to the relatively short measuring times, compared with the indium halflives. The halflives of the indium isomers were determined to $T_{1/2}(^{129}\text{In}(1/2^-)) = 1260 \pm 100$ ms and $T_{1/2}(^{129}\text{In}(9/2^+)) = 690 \pm 70$ ms. No MINOS errors could be obtained from this fit. The errors given are based on parabolic errors equipped with safety margins. At 100 ms after the start the number of neutron-emitting nuclei from the respective isotopes were $\#(^{129}\text{In}(1/2^-)) = 2\,058\,000$ and $\#(^{129}\text{In}(9/2^+)) = 882\,600$. This gives the ratio 2.3 ± 0.2; this figure can vary somewhat with collection time.
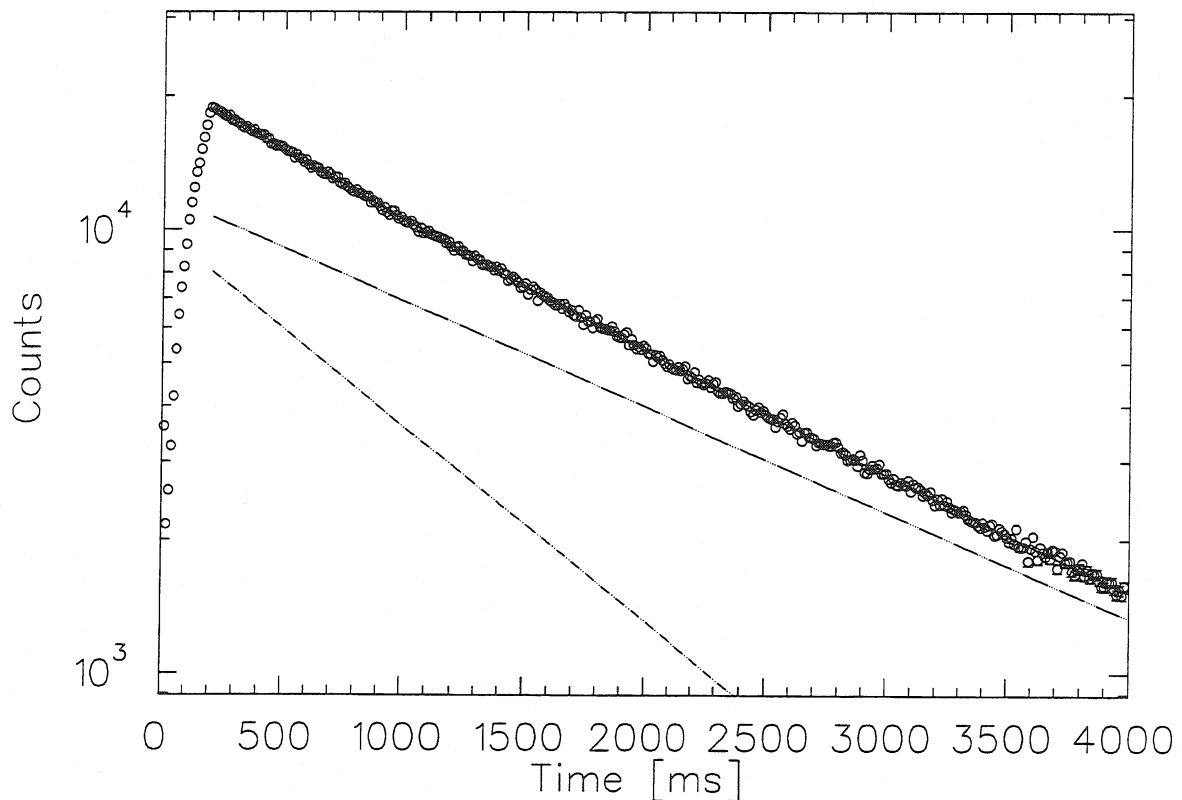

Figure 4.10: Beta-delayed neutrons from ^{129}In. The upper, longer component originates from the $1/2^-$ isomer and the lower from the $9/2^+$ ground state.

4.3.6 Production rates

This section will be used for a comparison of the measured yields for the two beamtimes and will be ended with a discussion of what yields would be needed to detect ^{129}Ag.

The "number of neutrons" in Tables 4.5 and 4.6 are the total number of neutrons to be emitted from the nuclei existing 100 ms after the measurement started. This number is based on the observed decay. The uncertainties in the total number of neutrons are the MINOS errors when those could be obtained. For masses 128 and 129 MINUIT could only determine parabolic errors. The neutrons per pulse are the "number of neutrons" divided by the number of cycles in the respective spectra. The neutrons per pulse has also been shown in Figure 4.11.

Table 4.5: Absolute neutron production per pulse - IS333 June 1994

Isotope	Collection time [ms]	Cycles	Number of neutrons			Neutrons/pulse		
^{121}Ag	300	385	53 000	±	3000	140	±	10
^{122}Ag	300	428	52 000	±	1000	120	±	5
^{123}Ag	300	2645	18 000	±	500	6.8	±	1
^{124}Ag	300	3937	22 000	±	500	5.6	±	0.5
^{125}Ag	300	2933	7500	±	500	2.6	±	0.5
^{126}Ag	100	6614	1200	±	100	0.2	±	0.05
^{127}Ag	100	25 067	1600	±	300	0.06	±	0.02
^{127}In	100	25 067	300 000	±	20 000	12	±	2

Table 4.6: Absolute neutron production per pulse - IS333 July 1995

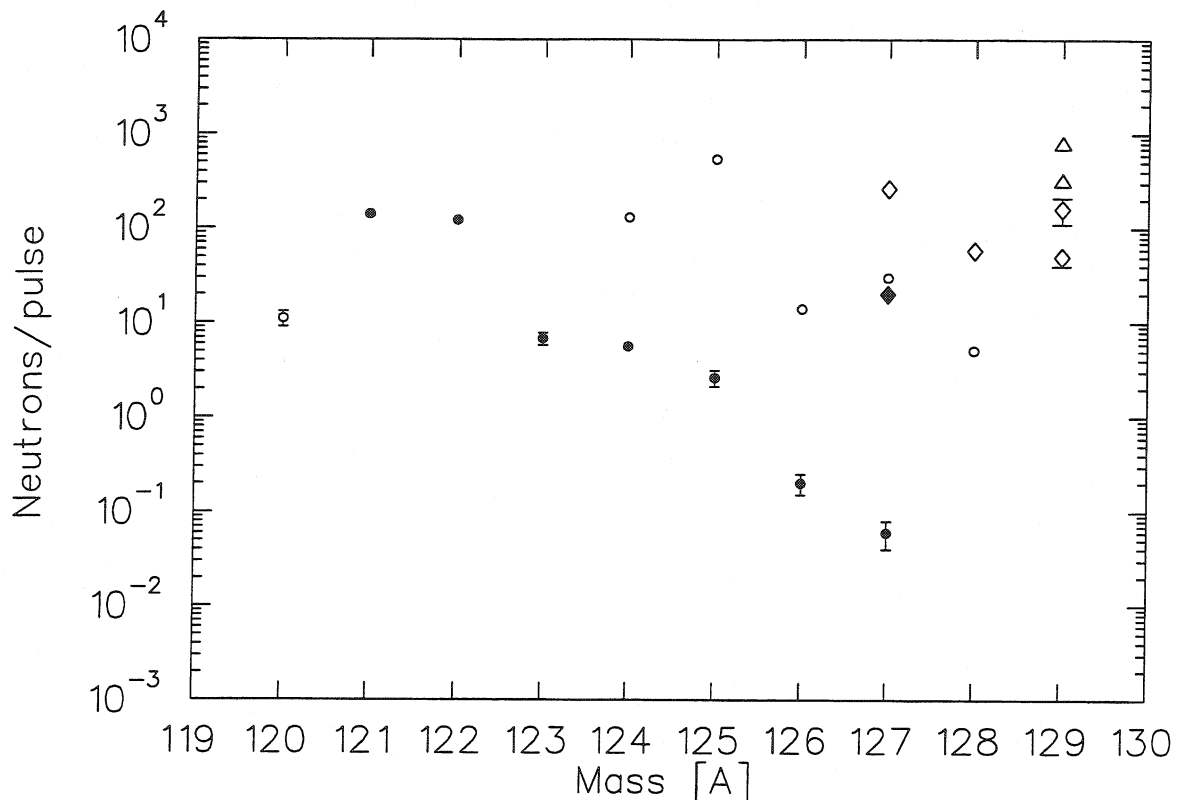| Isotope	Collection time [ms]	Cycles	Number of neutrons			Neutrons/pulse		
^{120}Ag	600	1412	16 000	±	2000	11	±	2
^{124}Ag	150	1283	166 060	±	460	130	±	1
^{125}Ag	200	425	229 100	±	740	540	±	2
^{126}Ag	150	2923	40 000	±	1000	14	±	1
^{127}Ag	150	2133	65 000	±	2000	30	±	2
^{127}In	150	2133	550 000	±	10 000	260	±	10
^{128}Ag	150	3935	20 000	±	1000	5.1	±	1
^{128}In	150	3935	230 000	±	5000	58	±	2
^{129}In(1/2$^-$)	200	2735	2100 000	±	100 000	770	±	50
^{129}In(9/2$^+$)	200	2735	850 000	±	50 000	310	±	25
^{129}In(1/2$^-$)	80	11645	1900 000	±	300 000	160	±	50
^{129}In(9/2$^+$)	80	11645	580 000	±	25 000	50	±	10

Figure 4.11: Compared number of neutrons per pulse for the two experiments; circles indicate Ag, quadrangles and triangles In isotopes. For mass 129 two In isomers were seen and data was taken with two different collection times. The triangles indicate the data taken with the longer collection time of 200 ms.

The number of neutrons per pulse is fairly well defined from the analysed spectra, within the given errors. However, one has to be aware that the conditions for the different spectra can vary quite considerably. The length of the collection time can have been changed for different masses and beamtimes. This influences not only the observed number of neutrons from Ag but also the Ag-to-In ratio. However, this effect is small compared to the uncertainties introduced by the laser operation. During the experiments, the laser power fluctuated and instabilities in the laser frequencies as well as in the overlap, in time and space, between the three laser beams were observed. The temperatures of the target and ionizer were independently varied during the beamtimes. The target temperature is additionally influenced by the number of proton pulses per supercycle, which also varied. In addition, the number of protons per pulse could vary up to 40% depending on how the PSB was working. This had a direct influence on the production rate. A rather uncontrolled combination of these factors is the reason for the large spread in the increase of neutrons per pulse in the experiments from 1994 to 1995, shown in Table 4.7.

For mass $A = 127$, the increase for Ag is very high but the uncertainties are also very big. The large error is the result of the fact that the measurement in 1994, although running over a very long time, had poor statistics and a high isobaric background of indium. I cannot find any other reason that the increase for this mass is so much higher than for the other masses. The indium ratio has only increased by a factor of 22 which gives an increase in the Ag-to-In ratio of a factor of $480/22 = 22$.

Table 4.7: Comparison of absolute neutron emission per pulse between the beamtimes in June 1994 and July 1995, for mass 124 - 127. The number of neutrons per pulse from 1995 has been divided with the corresponding number from 1994.

Isotope	Increase of neutrons per pulse 95 - 94			
^{124}Ag	$\dfrac{166060 \cdot 3937}{1283 \cdot 22000}$ =	23	$\pm$	0.5
^{125}Ag	$\dfrac{229100 \cdot 2933}{425 \cdot 7500}$ =	210	$\pm$	14
^{126}Ag	$\dfrac{40000 \cdot 6614}{2923 \cdot 1200}$ =	75	$\pm$	2
^{127}Ag	$\dfrac{65000 \cdot 25067}{2133 \cdot 1600}$ =	480	$\pm$	91
^{127}In	$\dfrac{550000 \cdot 25067}{2133 \cdot 300000}$ =	22	$\pm$	1.5

The first measurements at A = 127 from 1994 shows that it should be possible to see a short halflife component of some 100 ms if the In-to-Ag ratio in the first channel after closing the beamgate is > 50, possibly even 100. At mass 128 this ratio is about 1.4. Since no such short halflife component was observed as indication of ^{129}Ag, I assume that the In-to-Ag ratio for A = 129 was about 70. This gives a decrease in this In-to-Ag ratio from mass 128 to 129 by a factor of 50. The distribution of the production rates for Ag goes down rather steeply from A = 128 to 129, realistically by a factor of 100. The corresponding decrease for indium is about 10. The P_n value of indium increases by about a factor of 40. Looking at the indium isotopes with corresponding neutron numbers just before the full shell, no dramatic difference between ^{130}In$_{81}$ and ^{131}In$_{82}$ occurs. Based on this comparison, it is not to be assumed that the P_n value for ^{129}Ag would increase dramatically, compared to the value for ^{128}Ag. However, there is also no reason to belive that it would decrease. A realistic guess is that the P_n value for ^{129}Ag is at least as high as for ^{128}Ag.

Starting with the In-to-Ag ratio for ^{128}Ag of 1.42, taking changes in production rates as well as in P_n value into account, an In-to-Ag ratio of $1.42 \times 10 \times 40 \approx 600$ is obtained. This means that it is necessary to suppress indium another 10 - 15 times in order to be able to observe a short ^{129}Ag component.

Chapter 5

Neutron-rich nickel isotopes

In this chapter, facts concerning the attempt to produce neutron-rich nickel isotopes with a laser ion source at the CERN-ISOLDE facility have been summarized. The chapter begins with a discussion of reasons for carrying out this experiment. In the first section, the part treated in the greatest detail, the search for a suitable ionization scheme for nickel is discussed. These preparations were carried out in Mainz at the Institute of Nuclear Chemistry. This section is followed by a description of the experimental setup. The chapter ends with a summary of selected results and conclusions. This chapter does not claim to be a complete description of the nickel test but focuses mainly on the preparations made in Mainz. For more information, see [Jok96].

The goal of the test with laser-ionized nickel was primarily to be able to produce nickel isotope at the ISOLDE facility. Nickel is an element which is not available with conventional ion sources at the facility. Its ionization potential of 7.6 eV is, as in the case of silver, somewhat high for common surface ion sources. Neither plasma ion sources have shown to be suitable for ionization of nickel, as in these ion-source types the isobaric neighbours Cu and Ga are very strongly ionized. The test made with the laser ion source was an attempt to increase the ionization efficiency as well as the selectivity. If this was proven to be successful, the second step planned was to measure neutron-rich nickel isotopes and if possible to identify the doubly-magic ^{78}Ni and determine its beta halflife.

The reasons for wanting to gain experimental data on ^{78}Ni are manyfold. The fact that it is a doubly-magic isotope far from stability makes it a very interesting object. Experimental data on this isotope may give information about nuclear structure far from stability. Being a neutron-magic as well as a very neutron-rich isotope, it is also a waiting-point nucleus for the astrophysical r-process at N = 50.

5.1   Ionization scheme

In order to benefit from a laser ion source, LIS, it is necessary to find an efficient ionization scheme for the element of interest. Particularly favourable is ionization via an auto-ionizing state, AIS, which can increase the ionization rate considerably. Test experiments were carried out in Mainz to find out the optimum conditions for the ionization of nickel by using a laser setup similar to the one at ISOLDE. However, at the time only one pulsed
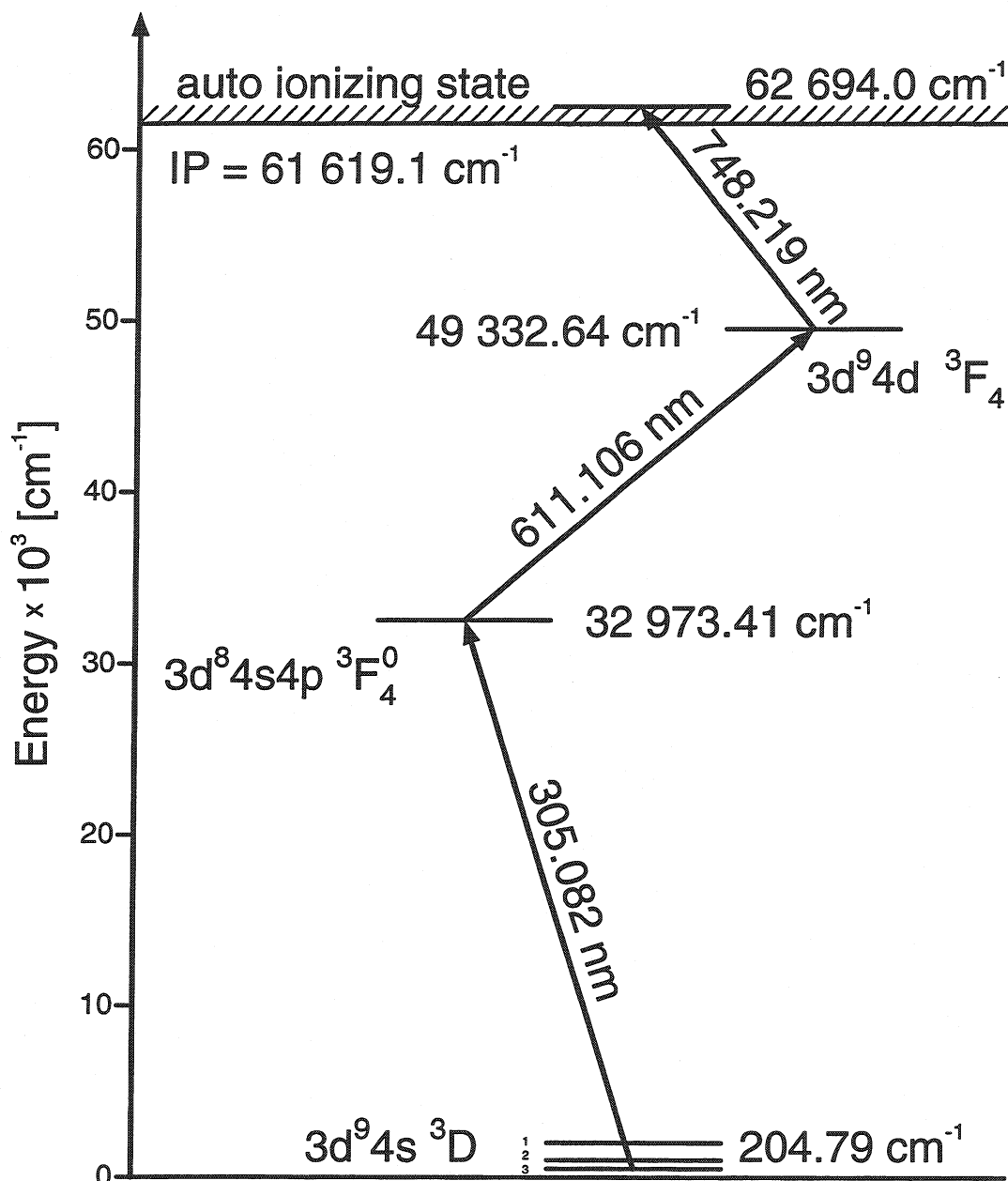
Figure 5.1: Ionization scheme for nickel used in the laser ion source at CERN-ISOLDE.

copper vapor laser was available to pump the three dye-lasers. For the search of a suitable ionization scheme, a nickel foil was heated to produce an atomic beam of nickel. The ions created in the interaction zone of the atomic beam with the laser beams were mass-selectively detected in a time-of-flight spectrometer, TOF.

The atomic level scheme of Ni contains several low-lying states [Moo71]. Due to an unfavourable transition probability, the ground state, which has a thermal occupation of 36% at 2500 K, was not used. Instead a level at 204.786 cm^{-1} was chosen which is occupied to 25% at this temperature; this is a representative working temperature for the LIS at ISOLDE. The first excited level populated with laser light of $\lambda_1 = 305.082$ nm was always the same, as it gave the most suited start for further transitions. This transition required

a frequency doubling with a non-linear BBO-crystal. For the second step, two different transitions were investigated. Initially, $\lambda_2 = 617.681$ nm was tested. For the search of an AIS, λ_1 and λ_2 were fixed and the third dye-laser wavelength was scanned through the continuum from 66 970 to 66 440 cm^{-1}, from 65 930 to 64 680 cm^{-1}, from 64 500 to 63 740 cm^{-1} and from 63 330 to 62 390 cm^{-1}. In these scans no AIS was found. However, there are several AIS tabulated close to the ionization potential, IP, but none which have the right parity for the transitions from the level obtained with $\lambda_2 = 617.681$ nm. Based on this information, a search for an AIS was performed close to the IP at 62 694.1 cm^{-1}. For this the wavelength for the second transition was changed to $\lambda_2 = 611.106$ nm. With this excitation scheme, an AIS for $\lambda_3 = 748.219$ nm was found at 62 694.1 cm^{-1}. In Figure 5.1 the applied ionization scheme is shown.

The first two transitions could be saturated with the available laser power. However, the interaction region where the three laser beams overlap with the atomic beam could not be well defined. This made the estimates of the saturation power for the three excitations a bit uncertain: $P_{laser}^{sat}(\lambda_1) \approx 65$ mW/cm^2, $P_{laser}^{sat}(\lambda_2) \approx 6000$ mW/cm^2 and $P_{laser}^{sat}(\lambda_3) \approx 9000$ mW/cm^2.

With the accuracy of the dye-laser width of 20 GHz, an isotope shift for nickel could be observed in the third step between the stable isotopes ^{58}Ni and ^{64}Ni. No isotope shift was observed in the second step where the dye-laser width was 30 GHz.

5.2 Experimental setup

The experiment was, like the silver experiment, carried out at the ISOLDE facility. This facility has already been described in this thesis as well as the principal setup of the lasers for the LIS. More information and further references are found in the corresponding sections.

5.2.1 Targets and ion sources

It was suspected that the release time of nickel from the target might be long. Due to this, a uranium target was used which has been especially developed for fast release in the Saint-Petersburg Nuclear Physics Institute. This uranium-di-phtalo cyanine or UDPC target has a chemical structure in the shape of hexagon rings. The target had a total uranium content of 7.6 g/cm^2. In order to be able to calibrate the frequencies of the lasers a mass marker of 9.4 μg of natural Ni was added to the target. The ionizer used was a standard surface tungsten capillary 30 mm in length, with an inner diameter of 3 mm and an outer diameter of 5 mm.

The second target that was tested was a Ta-foil target with a thickness of 93 g/cm^2, in combination with the same type of tungsten ionizer as above. Tantalum has a lower formation cross-section for nickel than uranium. However, if it has a faster release this disadvantage could be compensated.

5.2.2   Detectors

The experiment was carried out at the CERN-ISOLDE GPS. The mass-separated beam was implanted into a tape which transported the activity to the detectors. The detector setup consisted of a 4π plastic scintillator for beta measurements and high-purity Ge-detectors for gamma measurements.

The data was taken as beta- and gamma-singles spectra and $\beta - \gamma$-coincidences. The coincidences helped to confirm that the activity in the beta detector originated from nickel and not from isobaric contaminants.

5.3   Results and conclusions

The resonant photo ionization proved to be very powerful. To determine the selectivity of the laser ionization efficiency, measurements were carried out on the stable isotope ^{58}Ni. There the resonant ionization for the UDPC target was found to be ten times higher than the non-resonant ionization into the continuum. This latter measurement was made with the third laser blocked. The resonant ionization was some 4000 times more efficient than the surface ionization. As the first and second step were in saturation and the third close to being saturated, there is not much to be gained by increasing the laser power.

The difference between the laser ionization and the surface ionization was even bigger for the Ta target, where the photo ionization was some 10 000 times more efficient than the surface ionization.

The total release time from the target and ion source was measured by sampling the beta count rate as a function of time after the proton pulse. In this way, the release times for the tested targets were found to be to the order of 20 minutes, or even longer. An temperature increase to the maximum operation temperature of approximately 2500°C did not bring any improvements in the release speed. A last attempt to speed up the release by adding fluorine in the form of CF_4 was made. However, this was also without effect.

The absolute ionization efficiency was also measured for the unstable isotopes. This value is strongly dependent of the halflife as well as on the release time of the nuclei. For a long release time in combination with a short halflife the efficiency decreases. Due to this relation, the ionization efficiency was expected to be rather low because of the extremely long release times. The highest efficiency of 1.2% [Jok96] was found for measurements with ^{67}Ni from the UDPC target. This was not unexpected as that was the isotope with the longest halflife from those measured.

It has to be concluded that the extremely long release times of nickel for the tested targets makes the investigation of short-lived neutron-rich nickel isotopes impossible. Also with relatively good production rates in the target only a very small fraction of the isotopes will come out of the target before they have had time to decay.

Chapter 6

Concluding remarks

The experimental activity in the field of exotic nuclei has increased dramatically in the last years. The interest in this field can also be seen through the number of conferences and workshops being organized on this subject. This activity has led to an increase in the knowledge of what effects are important for the nuclear structure far off stability in different mass regions.

It is widely recognized that the proton-neutron, p-n, interaction holds an important position in the understanding of nuclear structure. This is also true for the $A \simeq 130$ region and the neutron-rich silver isotopes measured in this thesis. The monopole component of the p-n interaction directly influences the position of the individual single-particle, s-p, levels. Heyde has illustrated the importance of the monopole p-n interaction for the $\nu g_{7/2}$ neutron and the $\pi g_{9/2}$ proton levels [Hey88]. The wave-functions of these two orbits have a large overlap and thus a large attractive monopole interaction strength [Pit93]. Due to this, the $\nu g_{7/2}$ orbit gains extra binding energy, relative to the $2d_{5/2}$, $2d_{3/2}$, $3s_{1/2}$ and $1h_{11/2}$ orbits, when the $\pi g_{9/2}$ orbit is filled. This can be illustrated by comparing the experimentally determined neutron s-p levels in $^{91}_{40}\text{Zr}_{51}$, where the $\pi g_{9/2}$ is still empty, and $^{131}_{50}\text{Sn}_{81}$, where the $\pi g_{9/2}$ shell is complete. When taking the $3s_{1/2}$ as a reference state, it can be seen that the energy of the $\nu g_{7/2}$ level decreases by 2.8 MeV in ^{131}Sn compared to its position in ^{91}Zr.

The measured halflives of the isotopes $^{121-128}\text{Ag}$ (see Table 4.3) have been compared with the most recent calculations of nuclear properties from Möller, Nix and Kratz [Möl96]. These calculations are based on a QRPA (quasi-particle random-phase approximation) model that uses a folded-Yukawa potential and the Lipgin-Nogami approximation for pairing. In this calculation, an isospin dependent term is also introduced to simulate p-n interaction in a very simplistic way. Earlier shell-model calculations [Pfe94] have shown that the p-n interaction leads to longer halflives for the neutron-rich nuclei right below the N = 82 shell. The comparison between [Möl96] and the measured halflives (see Figure 6.1) shows that for the lighter silver isotopes the measured halflives are somewhat longer than the calculated ones. However, this changes when approaching the closed neutron shell at ^{129}Ag. For $^{126,127}\text{Ag}$ the experimental values are somewhat shorter than the theoretical predictions, but still in fair agreement. However, for ^{128}Ag the theoretical prediction becomes longer than for ^{127}Ag, an effect which has not been observed in the experiments. Correspondingly, the deviation for ^{128}Ag is rather large. For ^{129}Ag the theoretical calculations [Möl96] predict a halflife of 47 ms, which is well in agreement with the experimental
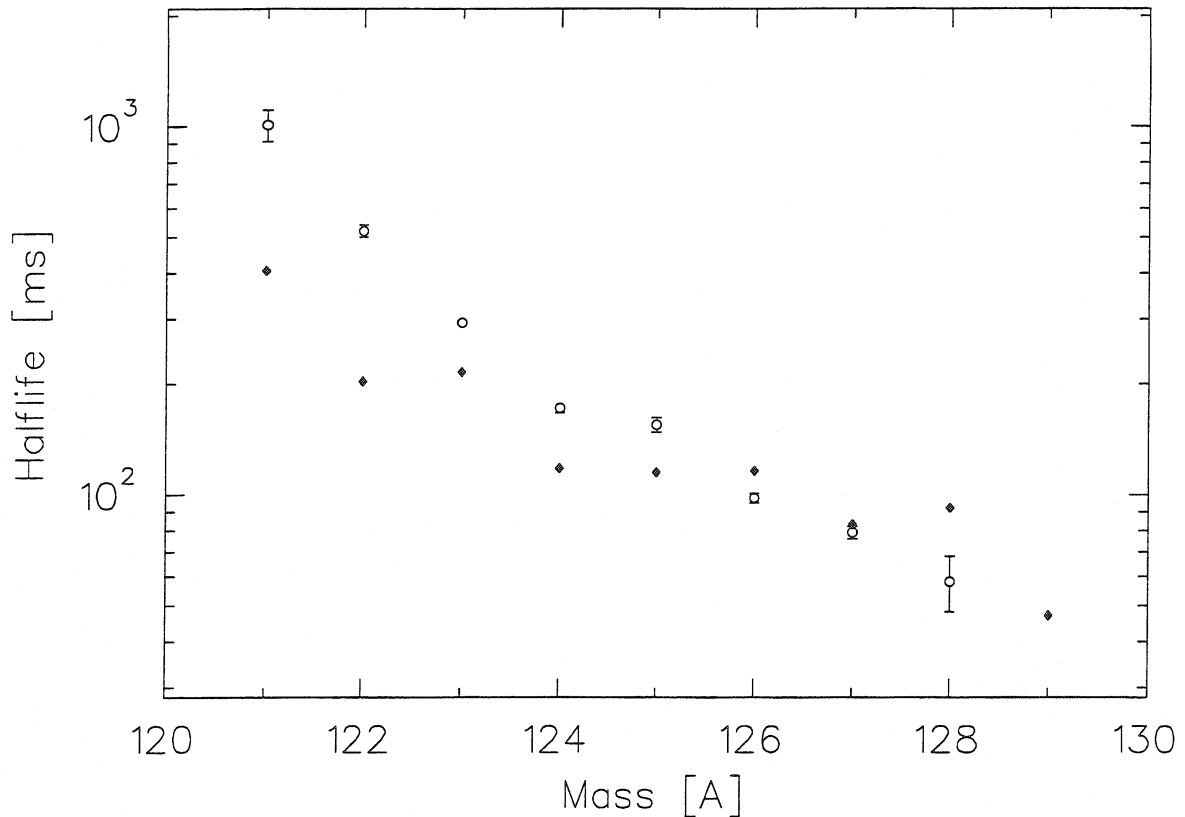
Figure 6.1: Comparison between the measured halflives and the most recent theoretical predictions from Möller, Nix and Kratz [Möl96]. The blank circles with error bars are the halflives measured in this work and the filled diamonds are the theoretical predictions using a folded-Yukawa potential.

trend from which one would expect a halflife of some 40 ± 10 ms for the neutron-magic ^{129}Ag.

As has been mentioned in the introduction, a direct connection between the r-process element abundances and the halflives of the progenitor nuclei exists. Consequently, a prediction of the halflife of the neutron-magic ^{130}Cd could be made, based on the r-process element abundances. Later experiments at the ISOLDE-SC confirmed this prediction [Kra86]. Encouraged by this progress, a similar attempt was made to predict the halflife for the next waiting-point nucleus ^{129}Ag. However, the QRPA calculations for this nucleus gave a halflife of only 17 ms which is too short to reproduce the solar ^{129}Xe abundance. Nevertheless, simulating the described effect of the p-n interaction by artificially lowering the $\nu g_{7/2}$ single-particle level by the interpolated value 2.1 MeV relative to the position given by the QRPA calculations, gave a halflife of some 140 ms. This resulted in a considerably improved reproduction of the solar ^{129}Xe r-abundance, in the A $\simeq$ 130 peak. However, extrapolating the trend of the experimentally-determined halflives in this thesis shows that $T_{1/2}(^{129}$Ag$) = 140$ ms for the ground state decay is a rather unrealistic prediction.

The apparent disagreement between the halflife predictions based on the experimental data and the one based on the solar abundances may, however, be solved. It seems that

the stellar situation requires that not only beta decay of the ground state has to be taken into account in this case but also the decay of an isomer. Using the QRPA calculations, one can also make a theoretical prediction of the isomeric decay halflife of a $\pi p_{1/2}$ proton in ^{129}Ag. Only taking pure Gamow-Teller decay into account gives a halflife of some 500 ms and when the first forbidden decay is considered, a value of 370 ms is obtained. Returning to the r-process calculations, the "stellar halflife" seems to be well reproduced by a mixture of the halflives from the ground state and the isomer. It is not enough to only take the thermal population of the $\pi p_{1/2}$ isomer into account, as the spin weight of the $9/2^+$ ground state is comparably high. Due to this, such an approach only gives an effect of some 5% for stellar temperatures of $T_9 = 1 - 2$. It seems that the situation for the neutron capture in ^{128}Ag can be well explained by capture in states above the S_n in ^{129}Ag. From these capture states γ-decay to both levels, $\pi p_{1/2}$ and $\pi g_{9/2}$, can occur and in this way the required stellar halflife would be described by a mixture of the $T_{1/2}$ from the two isomers.

Studying the Cd and In isotopes in the $N \simeq 82$ region, it can be seen that in most cases two and sometimes even three beta-decaying states have been observed. Also for the experimentally well known silver isotopes closer to stability, isomeric states are known. The heaviest silver isotope where an isomeric state has definitely been identified is ^{120}Ag. In the case of ^{122}Ag a certain confusion exists. However, as I have discussed in Section 4.3.2, I have not found any publication that experimentally supports an isomer. The gamma measurements made on ^{124}Ag decay during the beamtime in July 1995 imply that there may also be an isomer in this nucleus [Wal95]. Nevertheless, the fact that the lighter silver isotopes, in addition to the Cd and In isotopes in the $A \simeq 130$ mass region, have isomers implies that isomeric states should also exist in the heavy silver isotopes.

Evaluating the neutron data for $^{121-128}$Ag, no signature of more than one beta-decaying state could be found in these nuclei. All halflives could be well fitted with only one silver component and for the two heaviest isotopes one indium component. However, the fact that no isomers were observed in the beta-delayed neutron spectra does not mean that they do not exist. One possible, but rather unlikely, solution could be that only one state emits neutrons. However, fitting the indium components it can be seen that for ^{127}In the two halflife components of 1.12 s and 3.8 s respectively cannot be separated in spectra with measuring times as short as 4 s, even though their halflives differ by a factor of 3.4. For ^{129}In, the two halflife components of 0.68 s and 1.26 s respectively can be separated and it is not possible to fit them with one *total* component. This holds true even though the halflives only differ by a factor of two. The reason for this is without doubt that in ^{127}In one component is some 100 times weaker than the other. In ^{129}In, the difference in intensity is small, a factor of 2 - 3. These examples show that it is also possible that two or more neutron-emitting isomeric states can exist, but with unresolved halflives, especially if one component is very much weaker than the other. This can appear by large differences in P_n values or production rates, or both. It is also not possible to resolve halflives which are too similar to each other, as in the case of the two beta-decaying states in ^{128}In.

During discussions it has become clear that the reason for the missing isomers in the neutron-rich silver might be a totally different one, than the ones mentioned above. Mea-

surements on light silver isotopes as well as heavy indium isotopes, have revealed that the hyperfine structure of these isotopes is extremely dependent on the nuclear spin. Most light silver isotopes have a $1/2^-$ ground state configuration and show a rather moderate hyperfine splitting of a few GHz, which should be compared with the dye-laser width of 20 – 30 GHz. However, there is one outstanding exception and that is the $7/2^+$ isotope ^{103}Ag. For this isotope a hyperfine splitting of 40 GHz has been measured. In Section 3.2.2 I have shown that for a silver isotope with spin $9/2^+$ an even larger hyperfine splitting of 53 GHz may be present. As a consequence of such a large shift the laser ionization would no longer be as efficient as expected from the off-line measurements of stable silver isotopes. It could, as a matter of fact, even be very inefficient. In such a case, the very low production rates of the investigated isotopes can have to consequence that the ionization efficiency sinks below the limit where an identification is possible.

A hyperfine splitting of this size could explain that no isomers have been observed. The high-spin state would only be very inefficiently ionized while the low-spin state would still be well ionized. This could give the impression that only one state is present.

In addition, it has been discussed in Section 4.2 that the nuclear spin of the neutron-magic ^{129}Ag is probably $9/2^+$. Such a situation could naturally further complicate the identification of this isotope.

Chapter 7

Recent ion source tests and outlook

The somewhat unusual combination of subjects presented in this chapter is due to the fact that the ion source tests were carried out at a very late stage in the work for this thesis. The next IS333 beamtime is preliminary scheduled to take place at the ISOLDE facility during the fall of 1996. In the past winter shutdown period, a more powerful copper vapour laser tube has been installed. This will double the available power in the third photo ionization step and thus also increase the photo ionization efficiency by a factor of two. A new thyratron has also been installed which should improve the synchronization of the laser pulses.

During the same period, off-line ion source tests have been carried out. The off-line efficiency for silver with the previously-used Nb ionizer with a wall thickness of 1 mm was estimated at 10.8%. This has to be considered a fairly good efficiency for a LIS. Consequently, the primary goal of the further improvement of the ionizer is not to increase the efficiency. As the identification of the neutron-magic ^{129}Ag is still pending due to isobaric indium contamination, higher selectivity is now the most interesting improvement. The most promising approach in this direction is to speed up the release of the photo ionized silver from the ion source. In this way, an efficient microgating of the ion beam could be made between the 10 kHz laser pulses. This, however, presumes the release of a large fraction of the silver ions within some tens of μs. New off-line measurements at the HRS during the shutdown period have revealed that the photo ionized Ag is released in two peaks, where the prompt one was very short with a duration of a few μs, and the later main peak had a duration of some 25 – 30 μs. When applying a 30 μs gate over the main peak, the silver current decreased by 30 – 40%. This would decrease the indium current to 30% and increase the selectivity by about a factor of two.

A thinner Nb ionizer with a wall thickness of 0.5 mm has also been tested recently. This ionizer has an off-line efficiency for silver of 7.0%. However, the laser power in the ionization step was estimated to be a factor of two less compared to the efficiency measured above of 10.8% for the 1 mm Nb ionizer. The peak shape was found to allow 80% of the silver current to be emitted within a 20 μs gate. With this gate, the selectivity would increase by a factor of four. The construction of an even thinner Nb ionizer with a wall thickness of 0.25 mm is in progress. In order to prevent mechanical instabilities at high temperatures, supporting discs have been applied to these capillaries.

To further reduce the release time from the ionizer by increasing the extraction poten-
tial, a sapphire tube has also been tested. For this capillary, the voltage drop along the
tube is some 20 V. This can be compared with the 1 V which could be applied over the
1 mm thick Nb ionizer. Tests of this tube have shown that it has an ionization efficiency
for silver of some 2.3%. However, the efficiency is not stable when the source is heated.
During the tests it was observed that the photo ionized Ag was released in two peaks,
one prompt some μs long, and a main peak, with a pulse duration of some 10 μs. The
relative heights of the peaks vary with the temperature and quality of the vacuum. This
behaviour has not yet been fully understood. However, the main argument against this
source is that the indium ionization efficiency is too high at 4.6%, to be compared to
0.28% for the 0.5 mm Nb ionizer.

For the next beamtime it is also planned to use the newly installed high-resolution sepa-
rator, HRS, at the ISOLDE facility. In February 1996, the necessary hardware has been
installed which is needed to use a LIS at the HRS. When properly tuned, this separator
is expected to reach a mass resolution of M/ΔM = 30 000 [LPI93]. However, for the
experiment in 1996 a mass resolution of not more than 6000 – 7000 is predicted.

Nevertheless, the very promising ion source tests at the HRS reveal that the requested
improvement of the Ag-to-In ratio of, at least, a factor of 10 is not unrealistic. This should
be enough to detect ^{129}Ag isotopes.

The data acquisition should be changed from saving the data as single spectra to list
mode. This has the advantage that the β − n coincidences can be set during the off-line
analysis. In this way, it might be possible to identify the coincidences despite the high
rate of random coincidences caused by the large amount of beta particles.

In March 1996, tests were carried out to reduce the impact of the electronic noise from
the CVL. During the beamtime in 1995 these disturbances have proven to be the main
obstacle for the gamma measurements. Eliminating or at least minimizing this problem,
together with the use of the HRS, would make gamma measurements also possible on
silver isotopes heavier than ^{124}Ag. This would be a valuable complement to the neutron
measurements and could, for instance, clear the situation with the "missing" isomers. The
tests revealed that the disturbances seem to have decreased with the installation of the
new CVL tube, compared to the former setup. It was not possible to find any connection
between the degree of noise and the distance to the lasers. Further more, local resonance
phenomena were observed. A 5 μs gate was applied directly after the 10 kHz laser pulses
to the electronic modules of a simple gamma-detector setup. This arrangement made it
possible to take gamma data without electronic disturbances. The time-of-flight for the
silver ions through the separator is of the order of 30 μs, which is why the gate should
only reduce the silver current marginally.

During the next beamtime, it would also be desirable to investigate if the reason for the
missing isomers is indeed; that only atoms with nuclear spin 1/2$^-$ are ionized. This could
be done by detuning the laser frequency for the first transition according to the extrapo-
lated hyperfine splittings for the 7/2$^+$ and 9/2$^+$ configurations. This measurement could

be done with a gamma detector on an odd-A isotope with large production rates and well known gamma lines, for instance ^{115}Ag.

In a longer time perspective, the application of laser ion sources could further contribute to the understanding of the nuclear structure in the A $\simeq$ 130 region. Of special interest is the shell-model description around the doubly-magic $^{132}_{50}$Sn$_{82}$. In recent measurements at the ISOLDE facility the N = 83 single-neutron states in ^{132}Sn have been identified [Hof95]. To complete the picture, it would also be interesting to measure the still unknown single-proton levels in $^{131}_{49}$In$_{82}$. This could be done with gamma measurements in the beta decay of $^{131}_{48}$Cd$_{83}$.

Acknowledgments

I find it appropriate to start by thanking the person who first brought me to the idea of ever writing this thesis, Dr. Mats Rydehell.

The one person who has exerted the most influence on my thesis is without doubt my supervisor, Prof. Dr. Karl-Ludwig Kratz, I would herewith like to express my gratitude to him and to former and present members of his group for their inspiration and support. There are also many non-scientists in the Institute of Nuclear Chemistry in Mainz who deserve my gratitude for making my work and life easier in many ways during the years I have been working there.

Some Italians supposedly claim that this world is so hard that one needs two fathers to survive. Whether life as a German graduate student is as hard as the life on Sicily I cannot say. However, I would like to take the opportunity to also thank my co-supervisor Prof. Dr. Rainer Neugart.

During the development and application of a laser ion source for silver used at CERN-ISOLDE, I have had the privilege to work with scientists of many different specialities. In this context, I would like to take the opportunity to thank my colleagues from Troitsk Dr. V. Fedoseyev and Dr. V.I. Mishin; present and former members of the laser group in the Institute of Nuclear Chemistry and the EXAKT group in Mainz, Dr. R. Kirchner and Dr. H. Ravn as well as their colleagues at the GSI and CERN-ISOLDE, who, with their time, energy and intelligence have made this project possible.

I would also like to thank my collaborators and other physicists who shared their knowledge about experimental physics with me during experiments at ISOLDE and GANIL and at other times. Among those, I would especially like to thank Piet van Duppen for always having so many relevant questions and for letting me help him find the answers to some of them. The same thanks also goes to the former ISOLDE coordinator Olof Tengblad, for sacrificing time he did not have to help me with my experiments and for being a great guy to work with also in times of too little sleep. Thanks also to Karsten Riisager for sharing his knowledge on physics in general and analysis in particular with me. I am also grateful to Prof. Bill Walters for his inspiring and informative discussions and to Prof. Björn Jonson for the encouragement and support I have received since I have known him.

Last of all, thanks to my friends and family for supporting me during my "foreign exile".

Bibliography

[Ale78]   K. Aleklett, E. Lund and G. Rudstam, *Phys. Rev.* **C18** (1978) p. 462

[Awa79]   T. Awaya, *Nucl. Instr. Meth.* **165** (1979) p. 317

[Awa80]   T. Awaya, *Nucl. Instr. Meth.* **174** (1980) p. 237

[Bak84]   S. Baker and R.D. Cousins, *Nucl. Instr. Meth.* **221** (1984) p. 437

[Bee88]   H. Beer, F. Käppeler, N. Klay, F. Voß and K. Wisshak, *KfK Nachrichten* **1** (1988) p. 3

[B^{2}FH57]   E.M. Burbidge, G.R. Burbidge, W.A. Fowler and F. Hoyle, *Rev. Mod. Phys.* **29** (1957) p. 547

[DeG80]   L.-E. De Geer and G.B. Holm, *Phys. Rev.* **C22** (1980) p. 2163

[Dup92]   P. Van Duppen, P. Decrock, M. Huyse and R. Kirchner, *Rev. Scie. Inst.* **63** (1992) p. 2381

[Ead71]   W.T. Eadie, D. Drijard, F.E. James, M. Roos and B. Sadoulet, *Statistical Methods in Experimental Physics* North-Holland, Amsterdam (1971)

[Fed95]   V.N. Fedoseyev, Y. Jading, O.C. Jonsson, R. Kirchner, K.-L. Kratz, M. Krieg, E. Kugler, J. Lettry, T. Mehren, V.I. Mishin, T. Rauscher, H.L. Ravn, F. Scheerer, O. Tengblad, P. Van Duppen, A. Wöhr and the ISOLDE Collaboration, *Z. Phys.* **A353** (1995) p. 9

[Fee50]   E. Feenberg and G. Trigg, *Rev. mod. Phys.* **22** (1950) p. 399

[Fis75]   W. Fischer, H. Hühnermann and Th. Meier *Z. Phys.* **A274** (1975) p. 79

[Fog71]   B. Fogelberg, A. Bäcklin and T. Nagarajan, *Phys. Lett.* **36B** (1971) p. 334

[Fog76]   B. Fogelberg, L.-E. De Geer, K. Fransson and M. af Uggla, *Z. Phys.* **A276** (1976) p. 381

[Fog81]   B. Fogelberg, K. Heyde and J. Sau *Nucl. Phys.* **A352** (1981) p. 157

[Fog82]   B. Fogelberg and P. Hoff, *Nucl. Phys.* **A391** (1982) p. 445

[Fog84]   B. Fogelberg and J. Blomqvist, *Nucl. Phys.* **A429** (1984) p. 205

[Ful69]   G.H. Fuller and V.W. Cohen *Nucl. Data Tab.* **5** (1969) p. 433

[Gab87]   H. Gabelmann, *PhD Dissertation*, Institut für Kernchemie, Mainz Universität, Mainz (1987)

[Gra74]   B. Grapengiesser, E. Lund and G. Rudstam, *J. Inorg. Nucl. Chem.* **36** (1974) p. 2409

[Gök86]   H. Göktürk, B. Ekström, E. Lund and B. Fogelberg, *Z. Phys.* **324A** (1986) p. 117

[Hag92]   E. Hagebø, P. Hoff, O.C. Jonsson, E. Kugler, J.P. Omtvedt, H.L. Ravn and K. Steffensen, *Nucl. Inst. Meth.* **B70** (1992) p. 165

[Hai67]   F.A. Haight, *Handbook of the Poisson Distribution*, Wiley (1967)

[Han89]   P.G. Hansen and B. Jonson, "Beta-delayed particle emission from neutron-rich nuclei" in *Particle Emission from Nuclei III* CRC Press (1989) p. 157

[Hey88]   K. Heyde, "Nuclear Structure in the Zr region: Some Introductory Remarks" in *Nuclear Structure of the Zirconium Region*, Eds J. Eberth, R.A. Meyer and K. Sistemich, Springer Verlag (1988) p. 3

[Hil84]   J.C. Hill, F.K. Wohn, Z. Berant, R.L. Gill, R.E. Chrien, C. Chung and A. Aprahamian, *Phys. Rev.* **C29** (1984) p. 1078

[Hof95]   P. Hoff, P. Baumann, A. Huck, A. Knipper, G. Walter, G. Marguier, B. Fogelberg, A. Lindroth, H. Mach, M. Sanchez-Vega, R. Tayler, P. Van Duppen, A. Jokinen, M. Lindroos, M. Ramdhane, W. Kurcewicz, B. Jonson, G. Nyman, Y. Jading, K.-L. Kratz, A. Wöhr, G. Løvhøiden, T.F. Thorsteinsen and J. Blomqvist, to be published

[Huy83]   M. Huyse, *Nucl. Inst. Meth.* **215** (1983) p. 1

[Jad96]   Y. Jading and K Riisager *Nucl. Inst. Meth.* **A372** (1996) 289

[Jam95]   F James, Private communication

[Joh92]   N.L. Johnson, S. Kotz and A.W. Kemp, *Univariate Discrete Distributions* second edition, Wiley (1992) Chapter 4

[Jok96]   A. Jokinen, A.-H. Evensen, E. Kugler, J. Lettry, H. Ravn, P. Van Duppen, N. Erdmann, Y. Jading, S. Köhler, K.-L. Kratz, N. Trautmann, A. Wöhr, V.N. Fedoseyev, V.I. Mishin, V. Tikhonov and the ISOLDE collaboration; to be published

[Jon92]   B. Jonson and G. Nyman, "Beta-delayed particle emission" to be published in *Handbook of Nuclear Decay Modes*, CRC Press

[Kir78]   R. Kirchner and A. Piotrowski, *Nucl. Inst. Meth.* **153** (1978) p. 291

[Kir81]   R. Kirchner, *Nucl. Inst. Meth.* **186** (1981) p. 275

[Kir90]   R. Kirchner, *Nucl. Inst. Meth.* **A292** (1990) p. 203

[Kra83]   K.-L. Kratz, W. Ziegert, W. Hillebrandt and F.-K. Thielemann, *Astron. Astrophys.* **125** (1983) p. 381

[Kra86]   K.-L. Kratz, H. Gabelmann, W. Hillebrandt, B. Pfeiffer, K. Schlösser and F.-K. Thielemann, *Z. Phys.* **A325** (1986) p. 489

[Kra93]   K.-L. Kratz, J.-P. Bitouzet, F.-K. Thielemann, P. Möller and B. Pfeiffer, *Ap. J.* **403** (1993) p. 216

[Kug92]   E. Kugler, D. Fiander, B. Jonson, H. Haas, A. Przewloka, H.L. Ravn, D.J. Simon, K. Zimmer and the ISOLDE Collaboration, *Nucl. Inst. Meth.* **B70** (1992) p. 41

[LPI93]   "Laboratory portrait: ISOLDE PS-booster facility at CERN" *Nucl. Phys. News* **3** (1993) p. 5

[Lun76]   E. Lund and G. Rudstam, *Phys. Rev.* **C13** (1976) p. 1544

[Lun80]   E. Lund, P. Hoff, K. Aleklett, O. Glomset and G. Rudstam, *Z. Phys.* **A 294** (1980) p. 233

[Mac86]   H. Mach, R.L. Gill, D.D. Warner, A. Piotrowski, R. Moreh, *Phys. Rev.* **C34** (1986) p. 1117

[May92]   T. Mayer-Kuckuk *Kernphysik* Teubner, Stuttgart (1992)

[Mey92]   B.S. Meyer, G.J. Mathews, W.M. Howard, S.E. Woosley and R.D. Hoffman *Ap. J.* **399** (1992) p. 656

[MIN92]   F. James, *MINUIT reference manual*, version 92.1, CERN Geneva, Switzerland

[Mis93]   V.I. Mishin, V.N. Fedoseyev, H.-J. Kluge, V.S. Lethokov, H.L. Ravn, F. Scheerer, Y. Shirakabe, S. Sundell, O. Tengblad and the ISOLDE Collaboration, *Nucl. Inst. Meth.* **B73** (1993) p. 550

[Moo71]   C.E. Moore, *Atomic Energy Levels NSRDS-NBS 35, Vol II* US Department of Commerce, Washington (1971) p. 97

[Mos51]   S.A. Moszkowski, *Phys. Rev.* **82** (1951) p. 35

[Möl96]   P. Möller, J.R. Nix and K.-L. Kratz, submitted to *Atomic Data and Nuclear Data Tables*

[Nor80]   C. Nordling and J. Österman, *Physics Handbook*, Studentlitteratur, Lund (1980)

[Ohm81]   H. Ohm, *PhD Dissertation*, Institut für Kernchemie, Mainz Universität, Mainz (1981)

[Pfe94]   B. Pfeiffer, K.-L. Kratz, P. Möller, J.M. Pearson, J. Dobaczewski and F.-K. Thielemann, in *Proc. of the 4th Int. Conf. on Applications of Nuclear Techniques: "Neutrons and their applications" Crete, June 1994*

[Phi78]   G.W. Philips, *Nucl. Instr. Meth.* **153** (1978) p. 449

[Pit93]   S .Pittel, P. Federman, G.E. Arenas Peris, R.F. Casten and W.-T. Chou, *Phys. Rev.* **C48** (1993) p. 1050

[Rag89]   P. Raghavan *Atomic Data and Nuclear Data Tables* **42** (1989) p. 189

[Rav79]   H.L. Ravn, *Phys. Reports* **54** (1979) p. 201

[Ree83]   P.L. Reeder, R.A. Warner and R.L. Gill, *Phys. Rev.* **C27** (1983) p. 3002

[Råd84]   L. Råde and M. Rudemo, *Sannolikhetslära och statistik för Teknisk Högskola* Biblioteksförlaget Stockholm (1984)

[Sch93]   F. Scheerer, *PhD Dissertation* GSI Report March 93, ISSN 0171-4546

[Seg77]   E. Segrè, *Nuclei and particles*, second edition, W. A. Benjamin Inc, Reading, Massachusetts (1977)

[Shi78]   L.L. Shih, J.C. Hill and S.A. Williams, *Phys. Rev.* **C17** (1978) p. 1163

[SMT84]   *Standard Mathematical Tables* 27th edition, editor W.E. Beyer, CRC Press Inc. 1984

[Ten88]   O. Tengblad, *PhD Dissertation*, Chalmers Tekniska Högskola, Göteborg (1988)

[Wal95]   W.B. Walters, Private communication

[Wie80]   W.L. Wiese and G.A. Martin *Wavelengths and Transition Probabilities for Atoms and Atomic Ions*, NSRDS-NBS 68 (1980)

[Wu66]   C.S. Wu and S.A. Moszkowski, *Beta Decay* Wiley, New York (1966)

[Zam95]   N.V. Zamfir, R.L. Gill, D.S. Brenner, R.F. Casten and A. Wolf, *Phys.Rev.* **C51** (1995) p. 98

Name:	Ylva Jading
Geburtsjahr:	1964
Geburtsort:	Västervik
Nationalität:	Schwedisch

1971 - 1980	Neunjährige schwedische Grundschule, Västervik (Schweden).
1980 - 1983	Naturwissenschaftlicher Abschluss, Västerviks Gymnasium, Västervik (Schweden).
Januar 1984 - Juli 1985	Stellvertretender Geschäftsleiter, Pasta & Cheese Inc, New York, (USA).
August 1985 - Juni 1992	Studium als Diplomingenieur, Fachrichtung Physik, Chalmers Tekniska Högskola, Göteborg (Schweden).
September - November 1988	Feldstudie über Anwendungen von Sonnenenergie als Diplomarbeit, Nkinga (Tansania).
Juni - August 1989	Sommer-Student am Experiment PS202 (Jetset), CERN, Genf (Schweiz).
September - Dezember 1990	Beschleuniger-Operateur am Synchrocyclotron, CERN, Genf (Schweiz).
seit September 1992	Doktorarbeit am Institut für Kernchemie, Johannes Gutenberg-Universität, Mainz (Deutschland).